Rijksuniversiteit Groningen

Bachelor Thesis

Modelling the Gas Kinematics of Galaxies at High Redshift in 3D

Author:
B. Danzer

Supervisor:
P. Mancera Piña
F. Fraternali

Contents

1 Introduction

Deriving the kinematics of distant galaxies at high redshifts, and their implementation into fundamental scaling relations is essential to construct a coherent evolutionary picture of galactic systems across the history of the Universe. Some authors propose that there has been little development in galactic kinematics over the last 10 Gyr (to redshift $z \sim 2$), and that present-day disc galaxies are already kinematically mature and rotation dominated by $z \sim 1$, with no significant evolution of key scaling relations in this time-frame (Portinari and Sommer-Larsen 2007; Di Teodoro et al. 2016; Marasco et al. 2019). Furthermore, some research claims that even by $z \sim 2$ star forming galaxies already display ordered rotation, but with velocity dispersions higher by a factor of up to five than local equivalents (Förster Schreiber et al. 2006; Übler, H. et al. 2019). Most agree that in general, galaxies in the local universe are less turbulent, and more rotation-dominated that their high-redshift counterparts (Wisnioski et al. 2015; Übler, H. et al. 2019). Concerning the shape of rotation curves, the scientific community is also not in consensus. Some authors report findings of rotations curves decreasing with radius at high redshift, possibly due to pressure from the large velocity dispersions, or the fact that baryon fractions in the universe were higher than dark matter fractions at these high redshifts, sufficiently so to not provide the gravitational support that creates a flat rotation curve (Genzel et al. 2017). In contrast, other authors find rotation curves flat out to large radii, at least up to $z \sim 1$ (Di Teodoro et al. 2016).

Galaxies can emit several different emission lines, and by taking advantage of the Doppler effect we can reconstruct and visualise their rotation. The Doppler effect is a phenomenon by which radiation emitted by a moving body is compressed or stretched, due to a relative motion between the source and the observer. Velocity fields are constructed by measuring the Doppler shifts of a rotating galaxy at different locations. Unlike for local systems, neutral hydrogen (HI) observations become unfeasible at redshifts greater than $z > 0.2$ due to the low sensitivity of modern day instrumentation, and so Hα observations start to take precedence. Belonging to the so-called Balmer series of hydrogen emission lines, the Hα line is observed as a consequence of an electron falling from the level $n = 3$ to $n = 2$, and has a well-established rest-wavelength of 656.28nm. It makes for an excellent means of tracing ionised hydrogen in interstellar gas, as the line is commonly observed during the recombination of an electron with the nucleus after photo-ionisation as it cascades downward.

In the case of recombination lines, a robust method of measuring the relative motion of gas is Integral Field Spectroscopy (IFS), which allows us to obtain 3-dimensional data cubes of spectra from 2-dimensional fields of view (FOV) on the sky; signal from each pixel across the FOV is fed into a spectrograph, and the resulting images are stacked into the layered FITS file known as a data cube, where each channel contains the emission of the galaxy at a different wavelength. A data cube consists therefore of two spatial axes, and one spectral axis. The powerful tool that is spectroscopy, using the latest generations of Integral Field Units (IFU) allows therefore for the derivation of kinematic information on distant bodies in the universe through the measurements of the Doppler shifts of known spectral features on galaxies' emission spectra, for instance the Hα emission line.

As with low redshift galaxies, we can ultimately determine from the gas kinematics the matter components of high redshift galaxies, by modelling rotation curves and thus infer dark matter content (Begeman 1989; Übler, H. et al. 2019). In principle, both data cubes and velocity fields allow for the derivation of rotation curves. A rotation curve is simply a visualisation of how the rotational velocity varies with distance from the centre of a galaxy, which directly reflects the mass distribution in the galaxy, including that of the dark matter halo, since rotation is governed by gravitational potential (Haynes 1999). By classical Newtonian mechanics, in the regions where mass contribution becomes negligible, the rotational velocity should drop off with the square root of radius; what is known as Keplerian fall. Yet, we commonly observe the rotation velocities in massive spiral galaxies to become constant, often beyond relatively low radii. A flat rotation curve can only imply therefore that there exists additional non-luminous mass at larger radii (Shostak et al. 1973; Rubin et al. 1980; van Albada et al. 1985).

Furthermore, from derived rotation curves we can study the evolution of fundamental scaling relations such as the Tully-Fisher (TF) relation between stellar mass and rotation velocity (Verheijen 2001; Reyes et al. 2011; Di Teodoro et al. 2016; Übler, H. et al. 2019), and the so-called 'Fall relation' between stellar mass and stellar specific angular momentum (Fall 1983; Posti et al. 2018; Marasco et al. 2019). Some studies find evolution of the zero-point of the stellar mass Tully-Fisher relation in different high-redshift regimes (Tiley et al. 2016; Übler et al. 2017), and explain such a phenomenon with varying ratios of dark matter to baryonic mass in the early universe. Other authors find evolution in the more local universe, with shallower slopes of the Tully-Fisher relation found at redshift $z \sim 0.5$ compared with $z \sim 0$ (Boehm et al. 2004), while others find little or no significant evolution out to $z \sim 1$ (Di Teodoro et al. 2016; Marasco et al. 2019).

At low redshifts, determining accurate and high-resolution rotation curves and relations is usually not a problem, using the 21cm emission line of cold, neutral hydrogen (Verheijen 2001; Ponomareva et al. 2017). The main limitations of studying high-redshift galaxies manifest themselves as particularly low spatial resolution and low surface brightness in observations due to their great distance from us, with consequences including beam smearing (Bosma 1978), and the fore-mentioned in-applicability of HI observations.

Beam smearing is a phenomenon by which the size of the point-spread function (PSF) adversely affects the extraction of kinematic maps from the data cubes. The effects of beam smearing are greater exerted on galaxies where the PSF is of comparable size to the extension of the galaxy emission in the cube. Extracting kinematic parameters from beam-smeared velocity fields leads to a consequent degeneracy between rotation velocity and velocity dispersion, causing their under- & over-estimation respectively, and can be so severe as to misrepresent rotation-dominated galaxies as being dispersion dominated (Di Teodoro et al. 2016). At $z \sim 1-2$, galaxies typically have diameters of $1-2$ arcseconds, yet have very few resolution elements along the disc. The use of Adaptive Optics (AO) to overcome beam smearing (Förster Schreiber et al. 2018) is sometimes a viable option for studying high redshift galaxies, but the loss of signal that would come with it would not allow us to trace rotation at large radii.

In this study, we will use the software $^{3D}BAROLO$; an open-source software, designed and optimised to rather uniquely reconstruct and derive the kinematics of distant galaxies, particularly those with poor spatial resolution, provided that the signal-to-noise ratio of the data cube is sufficient (Di Teodoro and Fraternali 2015). The software ultimately derives a number of kinematic parameters for the data cubes, primarily the rotation curves and velocity dispersions out to different radii, by iteratively fitting three-dimensional tilted-ring models to the emission line observations. By such a model, multiple rings of different inclinations are generated, assuming that all emitting material at the given radius is confined to a thin disk. These concentric rings may have their own rotation velocities, inclinations and positions angles, among other parameters, depending on which the user specifies to fit, and which to fix. The reader can find more information about the performance of $^{3D}BAROLO$ in Di Teodoro and Fraternali (2015), and examples of the reliability of the kinematic parameters derived with $^{3D}BAROLO$ using low resolution data can be found in Di Teodoro et al. 2016; Iorio et al. 2017; Mancera Piña et al. 2020.

Throughout this study, we adopt a flat ΛCDM cosmology with $\Omega_{m,0} = 0.27$, $\Omega_{\Lambda,0} = 0.73$ and $H_0 = 70$ km s^{-1} Mpc^{-1} (Ade et al. 2016), as in Di Teodoro et al. 2016 for consistency. Consequently for this configuration, 1" on the sky corresponds to 8.16 kpc at z = 1, with a look-back time of 7.8 Gyr.

2 Data Sample

In this thesis we use a small sample of four high-redshift galaxies; two at $z \sim 1$, and two at $z \sim 2$. The data cubes are taken from the K-band Multi-Object Spectrograph (KMOS3D, Wisnioski et al. 2015) and SINS/zC-SINF Spectrograph for INtegral Field Observations in Near Infrared (SINFONI, Förster Schreiber et al. 2018) galaxy surveys. A collection of both ground and space based observations, the KMOS3D survey released 739 unique data cubes of a homogeneous sample of galaxies around the peak of cosmic star formation (see Madau and Dickinson 2014), observed over almost a month using the Very Large Telescope (VLT), along with a catalogue containing some basic derived properties for each one. The SINS survey is the product of over 280 hours of observations at the VLT, primarily tasked with investigating the dynamics and properties of Active Galactic Nuclei host galaxies, through multiple emission lines including Hα. It is the largest survey of gas kinematics in the region $z \sim 2-3$; only approximately 30% of this sample had been observed in the Near Infrared (NIR) previously.

The two galaxies at redshift $z \sim 1$ are taken from KMOS3D, while the other two at redshift $z \sim 2$ is taken from SINS. All four have F160W HST images[1] corresponding to rest-frame I-band at $z \sim 1$, and rest-frame V-band at $z \sim 2$. Figure 1 shows the HST images of the galaxies, with contours overlaid at multiples of the rms noise in the image (Table 2). The galaxies were chosen because while they are poorly resolved, they seem to have a sufficient signal-to-noise ratio that we may confidently identify emission regions and study them. The size of the PSFs are roughy equal to their respective extensions on the semi-major axes, and so beam smearing is a significant hindrance to two-dimensional modelling, highlighting the importance of our three-dimensional approach. The galaxies COS3_18434, GS4_37124, and ZC407302 were chosen because they appear to have a signal-to-noise ratio sufficient to the requirements for the kinematic modelling, and earlier inspection of previous studies (Genzel et al. 2017; Förster Schreiber et al. 2018; Übler, H. et al. 2019) confirmed that they appear to show the kinematic qualities of rotating discs. Unlike the other three galaxies in the sample, U3_5138 has been modelled using $^{3D}BAROLO$ in an earlier study (Di Teodoro et al. 2016), and thus will serve as a control to this study.

Table 1 gives some of the main properties of the sample. The values used for stellar mass have been taken from Wuyts et al. 2011 for COS3_18434, GS4_37124 & U3_5138, and Förster Schreiber et al. 2018 for ZC407302. In some cases, varying masses were found between different literature (Wisnioski et al. 2015; Rodrigues et al. 2016), and the differences between them have been interpreted as the respective errors (Table 1). For the two galaxies at redshift $z \sim 2$ we used a standard error of 30% in the mass, as none was given in the literature.

[1]Publically available from the Hubble archive: https://archive.stsci.edu/pub/hlsp/

Sample Properties					
Galaxy ID	Field	RA [h m s]	DEC [^{o} ′ "]	$Log(\frac{M_*}{M_\odot})$	z
COS3_18434	COSMOS	150:04:18.34	02:21:39.67	10.59 ± 0.18	0.907243
U3_5138	UDS	34:14:58.35	-05:15:07.6	9.72 ± 0.47	0.80905
GS4_37124	GOODS-S	53:11:34.47	-27:44:18.09	10.49 ± 0.15	2.43241
ZC407302	SINFONI	09:59:56.00	02:56:51.00	10.39 ± 0.15	2.18190

Table 1: Core properties of the galaxy sample.

We use a software known as *kvis*, a division of the $Karma$ software package (Gooch 1995) to view the galaxies for the first time, inspect the quality of the data cube, and derive some basic statistical information from them. The *kvis* package allows us to overlay axes and contours on the data cube, and cycle through the channel maps too see how the emission from the galaxy moves through different channels. This will be of further use when constructing masks for the channels, as we describe in section 3. In section 4 we provide the modelled channel maps for all of the galaxies. Note the pixel scale of the KMOS cubes is 0.2 arcseconds per pixel, whereas the SINS data set uses 0.05 arcseconds per pixel. All of the HST images have a scale of 0.05 arcseconds per pixel.

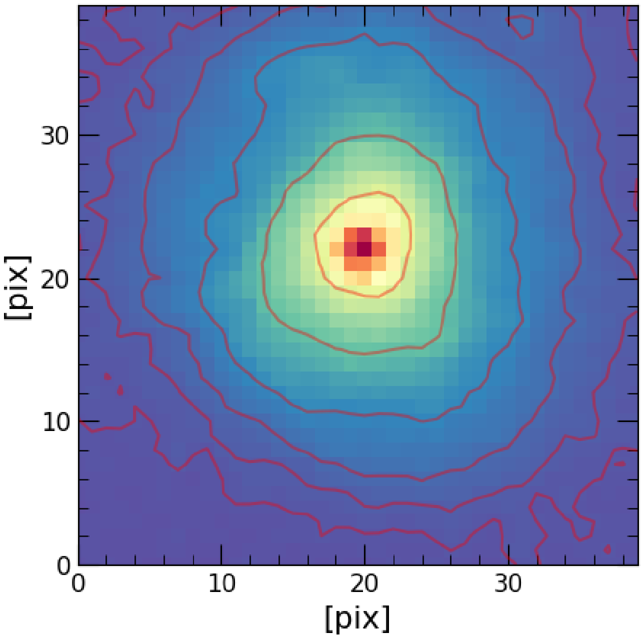

(a) COS3_18434

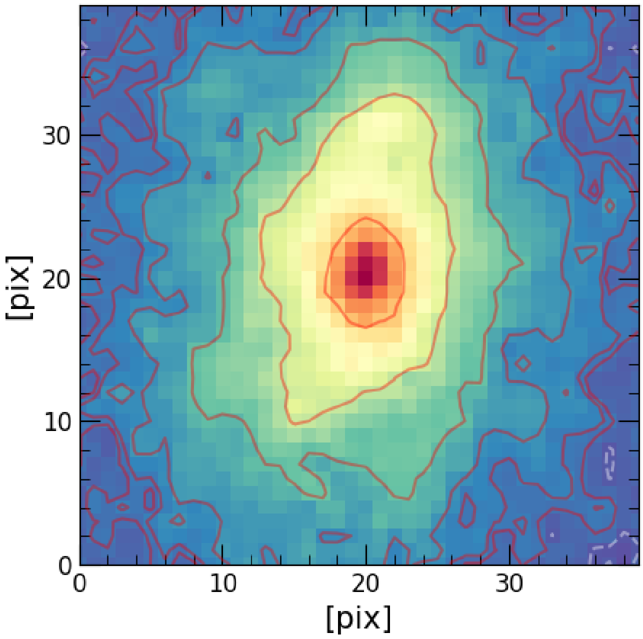

(b) U3_5138

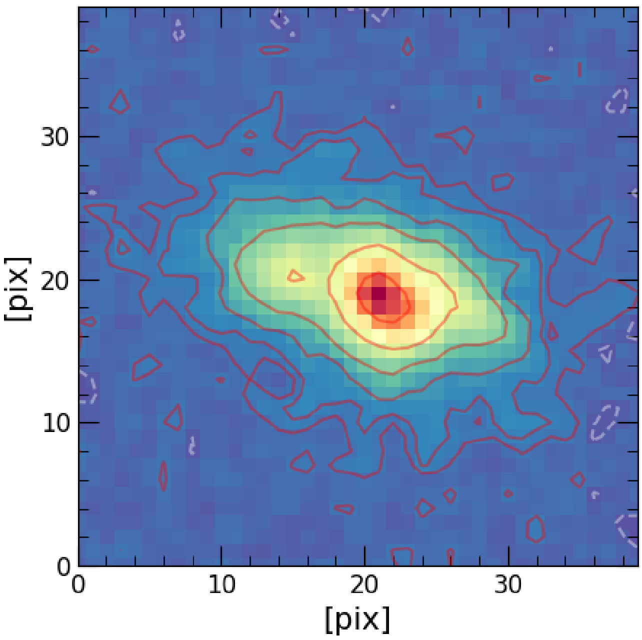

(c) GS4_37124

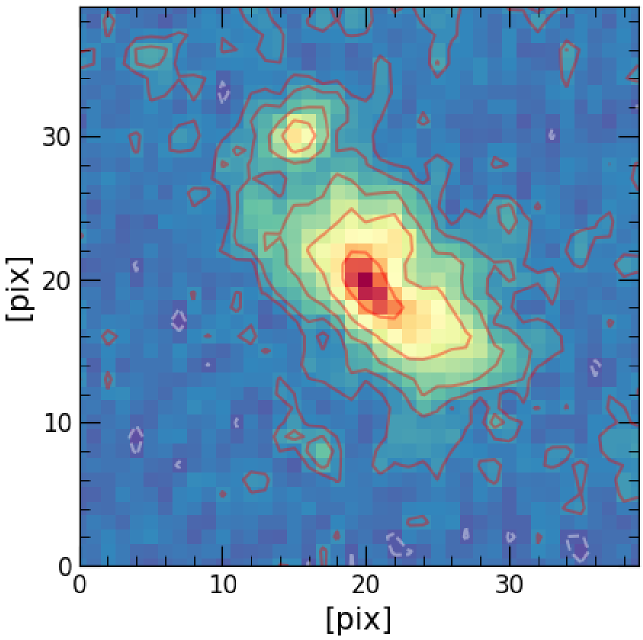

(d) ZC407302

Figure 1: HST images of the four galaxies in my sample, with red contours overlaid at levels of 2σ, 4σ, 8σ etc. up to 64σ, with one white contour plotted at -2σ. The upper two panels show the galaxies at $z \sim 1$, and the lower two at $z \sim 2$.

3 Methods

Prior to the kinematic modelling, it is necessary to perform a number of tasks to derive some basic geometric parameters to prepare the data, such as inclinations and position angles for the galaxies. ^{3D}*BAROLO* can estimate these parameters automatically, but for low-resolution data cubes such as those in this sample it is not always accurate.

3.1 Data Cube Inspection and Manipulation

The primary task performed in *kvis* was to identify the channels containing Hα emission. Typically this will consist of about 10-15 channels, and the rotation of the galaxy can be clearly traced when cycling through them (Figure 2b). It is essential to differentiate this region of Hα emission from the two adjacent regions in wavelength often visible either side of the Hα emission, in which you can observe the [NII] forbidden line emission (Figure 2c). The resolution between adjacent channels in the data cubes is given in Table 2.

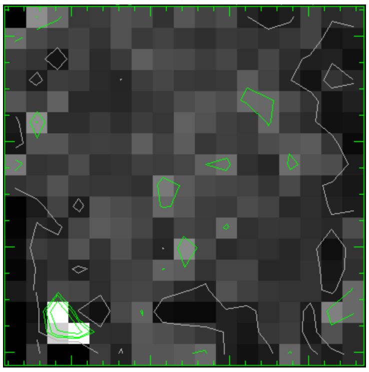

(a) A channel containing only noise.

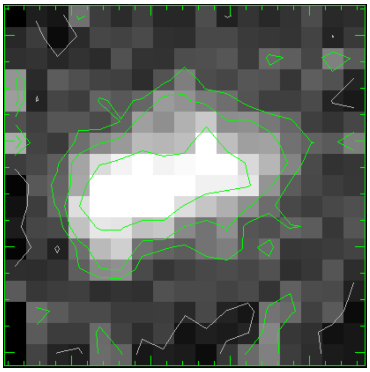

(b) A channel showing the galaxy in Hα emission.

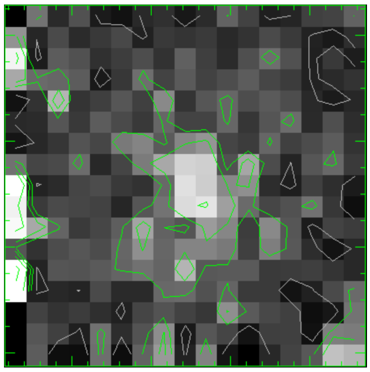

(c) A channel showing emission of the [NII] forbidden line.

Figure 2: Images taken from the *kvis* image viewer window of COS3_18434, overlaid with contours at multiples of 2σ, including one negative contour (grey contour) at -2σ.

Correctly chosen, contours help us to visualise the boundaries between galaxy emission and noise. The rms noise σ is calculated as the standard deviation of the brightness in an emission-free region. If we plot contours at multiples of 2σ for the galaxy COS3_18434, we can see it clearly on several channel maps (Figure 2b). Figure 2a shows a channel containing no Hα emission, and only noise.

Metadata stored in the FITS file headers needs to be manipulated to provide ^{3D}*BAROLO* with the information it requires to build the models. The headers of the cubes need to contain information on the PSF, namely the beam FWHM for both the major and minor axes, and its position angle. It was necessary to add to the header of the FITS file the name of the object that we are modelling for use in output plots, a rest frequency/wavelength of the spectral feature with which we are concerned (Hα), and the name of the telescope used.

Given that the data cubes contain over 2000 channels and our galaxies were emitting in 15-20 on average, we sliced the data cubes so that they spanned approximately $\pm$10 channels either

Data Cube Information			
Galaxy	σ $[10^{-20} m^{-2} \mu m^{-1} W]$	Channel Spacing $[km\ s^{-1}]$	Scale [kpc / "]
COS3_18434	8.4	27 - 46	7.943
U3_5138	2.2	27 - 46	7.65
GS4_37124	2.2	27 - 46	8.35
ZC407302	3.6	30 - 71	8.507

Table 2: Information derived using *kvis* on each of the data cubes in my sample.

side of those containing the galaxy emission. A cube with around 40 channels can be modelled in $^{3D}BAROLO$ in under 30 seconds, whereas the whole cube would have taken several minutes. Accurate kinematic modelling requires many iterations with fine tuning and adjustment, and so an efficient program is essential. The above-mentioned procedures were carried out in Python using the package *spectral_cube* in conjunction with *Astropy* (Price-Whelan et al. 2018).

3.2 The Point Spread Function

Information on the PSF size for each of the data cubes could be found in the headers of the first extensions of each of the FITS files, and could be read using *Astropy* routines. Prior to publication of the data cubes, the PSF for each pointing had been modelled by the survey teams with both a two-dimensional Gaussian and Moffat distribution, and the major & minor FWHM values (BMAJ/BMIN), as well as position angles (BPA), had been encoded into the headers of the data cubes. To confirm the accuracy of the PSF sizes given, we fitted two-dimensional Gaussian distributions to these PSFs using *Python*, and found results comparable to those given in the headers, as shown in Table 3. The PSFs found in our models are not too dissimilar to the values given in the cubes, yet they seem to be marginally, systematically smaller. For the galaxies U3_5138 and ZC407302, where the beams are almost circular, the BPA values differ more between the given and fitted values as the angle is harder to constrain. The BPA is much better constrained for the other two PSFs, with more elliptical shapes. We assume our methods to be less robust however, and will therefore use the survey parameters in our kinematic models. Figure 3 shows the PSF models plotted with the corresponding data, and residuals, with the modelled PSFs overlaid as black ellipses.

PSF Information						
	Given			Fitted		
Galaxy	BMAJ ["]	BMIN ["]	BPA [deg]	BMAJ ["]	BMIN ["]	BPA [deg]
COS3_18434	0.7615	0.6073	-8.0026	0.7296	0.5386	-7.5723
U3_5138	0.7930	0.7094	0.0041	0.5921	0.5198	27.5601
GS4_37124	0.7234	0.6126	-90.0	0.5959	0.4546	-90.0
ZC407302	0.1600	0.1600	0.0	0.2055	0.1831	76.7243

Table 3: Information on the PSF, given in the header objects of the galaxy FITS files and those derived in this study by fitting two-dimensional Gaussian functions.

3.3 Isophote Modelling

Essential to the kinematic models are the position angles and the inclinations of the galaxies. The inclination is of greater concern, as small errors at low inclinations $i \leq 30^o$ can propagate to much greater uncertainties in the rotation curves, as rotation is corrected by a factor $\sin{(i)}^{-1}$. At low inclinations there is a smaller rotational component along the line of sight (Di Teodoro et al. 2016). $^{3D}BAROLO$ is capable of estimating these parameters, yet again due to the poor resolution in the cubes we decided to estimate these parameters ourselves, making use of the HST images of the galaxies.

Position angles and inclinations of the galaxies are estimated by fitting a series of elliptical isophotes to the HST images of the four galaxies as shown in Figure 4. The Python module *Photutils* provides methods to fit concentric ellipses to a FITS image, provided with an initial ellipse guess, and determine best-fit parameters for ellipticity, and position angle, to name a couple. The ellipticity of an ellipse is related to the ratio between major and minor axes by $e = 1 - \frac{b}{a}$, where e is the ellipticity, and b & a are the major and minor axis lengths respectively. Figure 5 shows a graphical representation of the parameters derived, where black lines represent the outer ellipses, green horizontal lines show values given or guessed from literature, where applicable, and horizontal red lines present the median values of the outer ellipses. The inclination can then be estimated using the equation:

$$cos^2(i) = \frac{\left(\frac{b}{a}\right)^2 - \alpha^2}{1 - \alpha^2} \tag{1}$$

where α is the intrinsic axial ratio, for an edge-on system. Across different studies, authors have used a range of values for α depending on the assumptions made about the galaxy sample. If one were to assume infinitely thin disks, a value of $\alpha = 0$ should be used. In reality discs have non-zero scale heights and consequently a value of $\alpha = 0.2$ is often used, as will be adopted in this thesis.

Shown in Table 4 are the results for the isophote models made with the HST images of the galaxies. For fitting inclination, we are more concerned with the outer rings of the ellipse

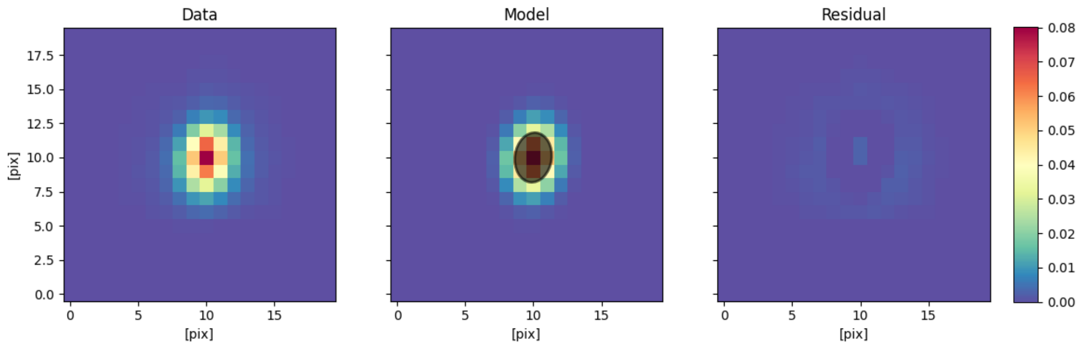

(a) COS3_18434

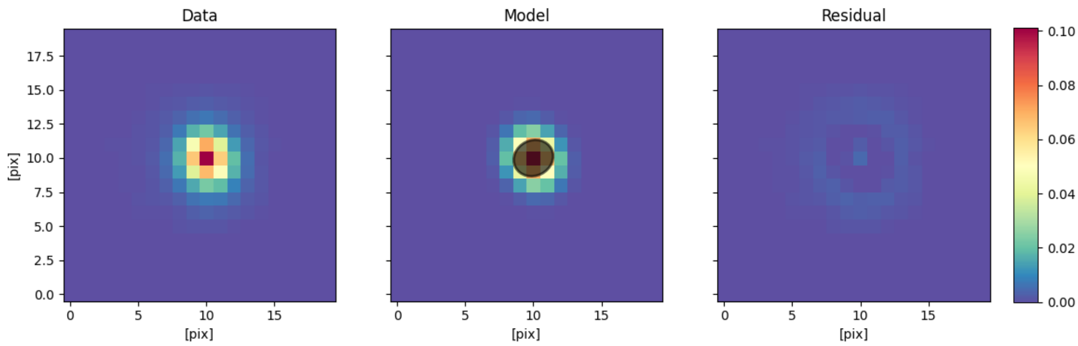

(b) U3_5138

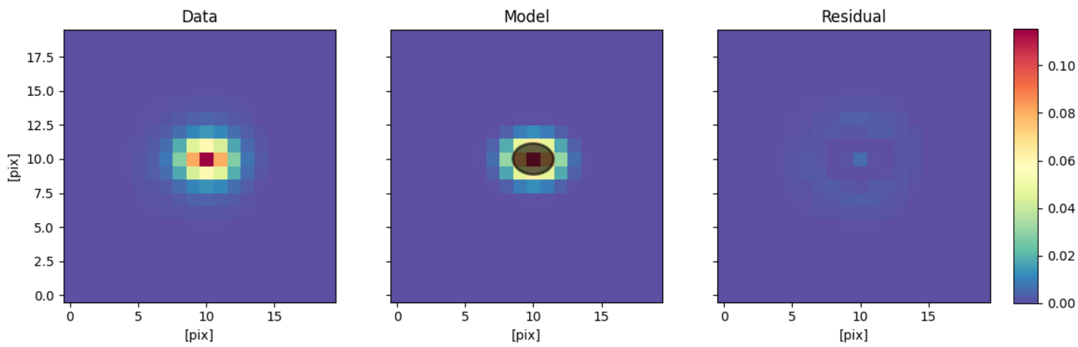

(c) GS4_37124

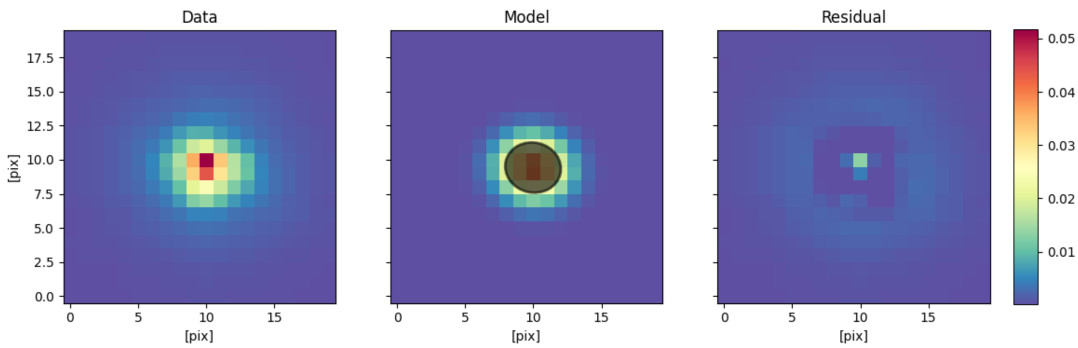

(d) ZC407302

Figure 3: Two-dimensional Gaussian functions fitted to each PSF. The PSF FWHM obtained from the model is plotted as the black ellipse.

models. The inner regions are dominated by very bright emission, some of which may just be bright star-forming regions and thus we derived these geometric properties from models of the outer rings that should be free of such a bias. In each case, the point beyond which the ellipses were considered to be 'outer' ellipses was determined manually, by visually inspecting the HST images with ellipses overlaid, and deciding where the emission was sufficiently dim. The errors in position angle and inclination are taken as half of the fitted range, in the outer ellipses (Figure 5).

Isophote Modelling						
	Literature		Fitted			
Galaxy	PA [deg]	i [deg]	PA [deg]	i [deg]	sin(i)	$R_d [kpc]$
COS3_18434	25	-	11.8 ± 11.2	35.7 ± 3.5	$0.584^{+0.049}_{-0.051}$	1.71 ± 0.03
U3_5138	-14	62	-11.5 ± 7.0	53.6 ± 3.4	$0.805^{+0.034}_{-0.037}$	2.97 ± 0.04
GS4_37124	250	-	249.6 ± 12.0	57.0 ± 7.9	$0.839^{+0.067}_{-0.083}$	2.19 ± 0.04
ZC407302	56	65.5	44.6 ± 4.7	63.7 ± 1.1	$0.896^{+0.009}_{-0.009}$	3.33 ± 0.20

Table 4: Parameters derived by the fitting of elliptical isophote models to the HST images of the four galaxies, and where applicable, corresponding literature values for PA and i. Position angles from literature were guessed from the velocity field output plots (as no values were given in tables) in Übler, H. et al. 2019 for COS3_18434 & GS4_37124, Di Teodoro et al. 2016 for U3_5138, and Förster Schreiber et al. 2018 for ZC407302. Scale lengths were derived assuming exponential surface brightness profiles.

The above procedure was found to be more effective for galaxies at higher inclinations, which is apparent for the galaxy COS3_18434. Figure 4a shows how the galaxy appears to be almost face-on, and the elliptical model generated by the program is actually almost circular. Consequently, the estimates for the position angle vary massively between the ellipses.

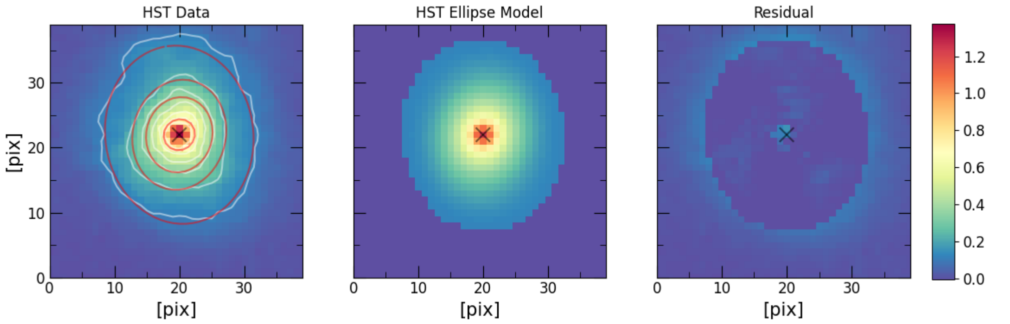

(a) COS3_18434

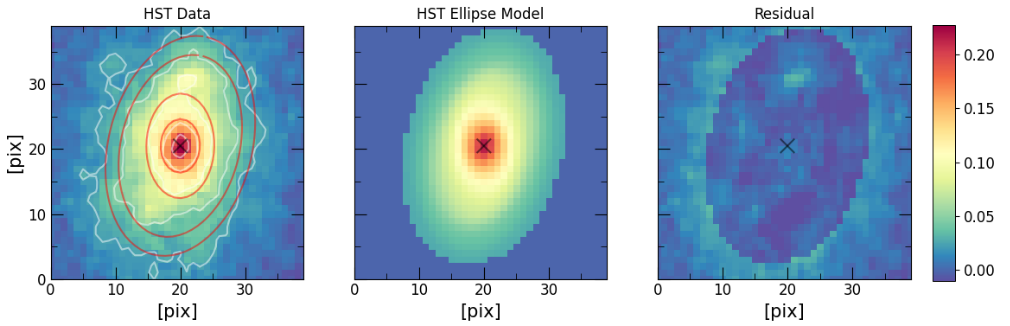

(b) U3_5138

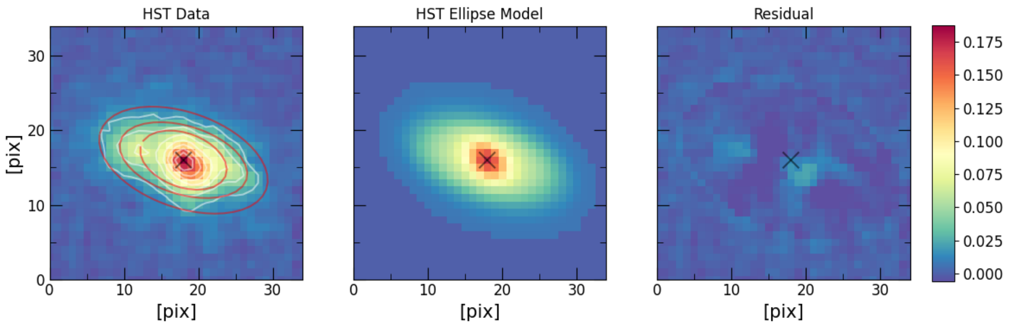

(c) GS4_37124

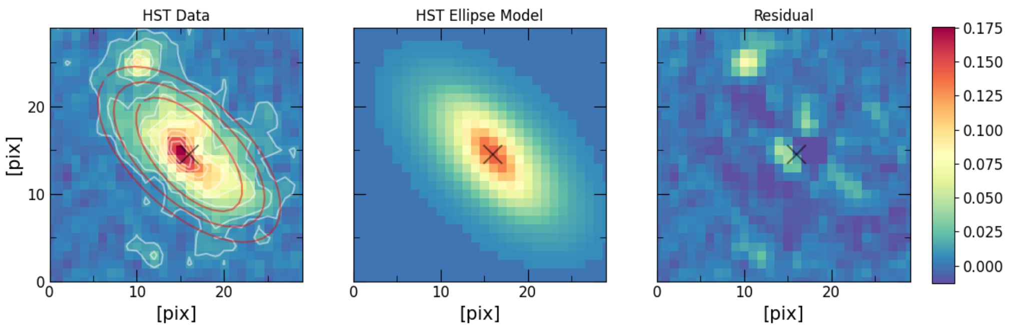

(d) ZC407302

Figure 4: Elliptical isophote models fitted for each galaxy in the sample. The fixed centres are shown by the black crossed. The panels from left to right show the HST image, overlaid with contours at multiples of the signal-to-noise ratio and the closest ellipses, the elliptical model built, and the residual between them.

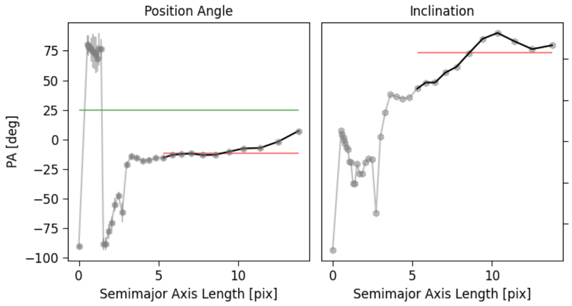

(a) COS3_18434

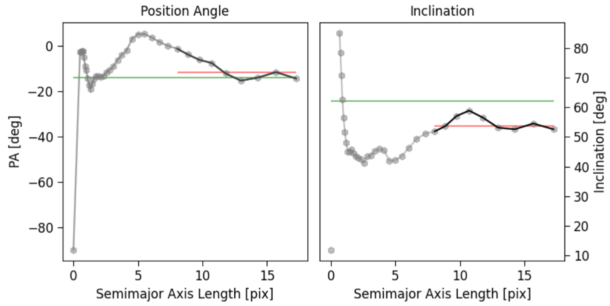

(b) U3_5138

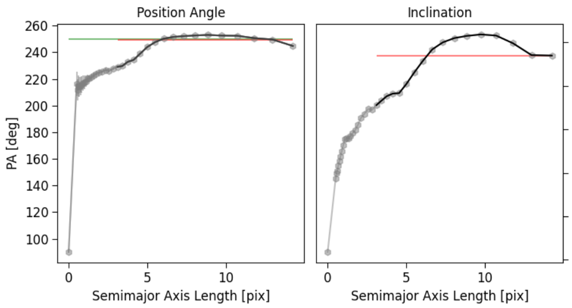

(c) GS4_37124

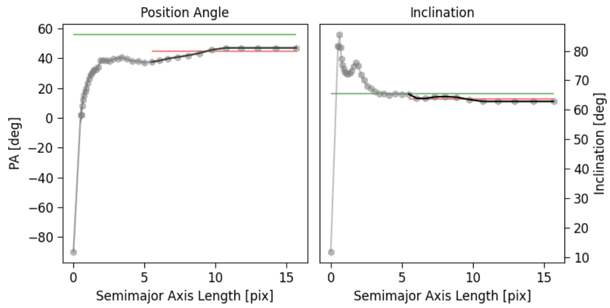

(d) ZC407302

Figure 5: Graphical representation of the parameters obtained from the fitted isophote models. Where applicable, green horizontal lines represent literature estimated values for the parameter, and red lines horizontal lines the median value of the outer ellipses (black lines).

3.4 Surface Brightness Profiles

An exponential profile shows how the surface brightness of a galaxy varies with radius from the centre, and has the following general form:

$$I(R) = I_0 * \exp\left(-\frac{r}{R_d}\right), \tag{2}$$

where r is the radius, I_0 is the central surface brightness, and R_d is the scale length of the disc. Figure 6 shows an exponential profile fitted to the surface brightness profile along the semi-major axis of each galaxy as solid coloured lines. The surface brightness profile along the semi-major axis is obtained through the HST isophote models. The dotted lines show the data points, extracted from the elliptical isophote models (section 3.3). The vertical lines, and the bars around them show the scale length from the fitted profiles, and their statistical errors. The exponential surface brightness models follow the data well in general, and the derived values can be found in Table 4. The profile for the galaxy ZC407302 does not drop off as quickly as the data does, and does not appear to be an ideal fit considering the data profile seems very similar to that of GS4_37124; hence the larger error for its scale length. Note that the central surface brightness for the galaxy COS3_18434 is around one magnitude higher than that of the other three, as given in the HST image. The errors in surface brightness are also taken straight from the isophote models, and are present in Figure 6, just too small to see in most cases.

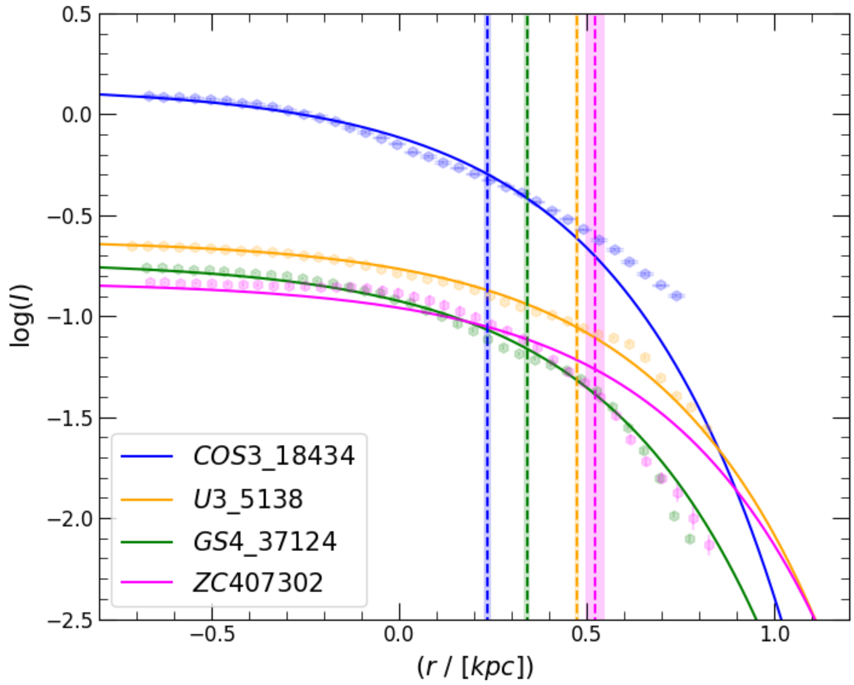

Figure 6: Exponential surface brightness profiles fitted to the surface brightness along the semi-major axis of each galaxy. Vertical lines and the bars around them represent the scale lengths and their statistical errors derived from the fitted profiles.

3.5 Kinematic Modelling with $^{3D}BAROLO$

To run $^{3D}BAROLO$, it is necessary to write a parameter file, in which users can specify certain parameters to fit or fix, provide initial guesses for others, and customise the way the program runs. $^{3D}BAROLO$ uses a three dimensional source-finding algorithm to automatically find the source in a data cube, which it then uses to construct a mask, and identify a centre if one has not been specified in the parameter file, using flux-weighted averages (Di Teodoro and Fraternali 2015). The source detection can be manipulated by specifying parameters THRESHOLD and GROWTHRESHOLD in the parameter file, in the same units as the flux in the data cube. Setting the MASK parameter to SEARCH tells the program to construct a mask using the detection from the source finding algorithm; if nothing is specified, the program will use all pixels with a flux greater than zero. If no parameter file is used, $^{3D}BAROLO$ can be run automatically on data cubes, but this procedure is often inaccurate for low-resolution cubes.

An issue encountered earlier on whilst attempting to fit particularly noisy galaxies with $^{3D}BAROLO$ was that the low signal-to-noise ratio in the data meant that much of the noise surrounding the galaxy emission was being interpreted as genuine galaxy emission by the program. Unable to resolve the issue by varying the source-finding or mask-making parameters fore-mentioned, the problem was overcome by manually constructing a mask to cut off the noise-dominated regions surrounding our galaxies in the data cubes. This was done by visually analysing each channel and identifying the areas that could be regarded as genuine emission. The concept of a mask is very simple. It is a FITS file of the same dimensions as the data cube, in which pixels that correspond to noise pixels in the data are set to zero and thus excluding them from the model, whereas the pixels containing genuine emission in the data cube have corresponding values of one in the mask. The original data cube, and the mask cube are then multiplied together. The purpose of a mask is simply to exclude regions of noise from the fitting, so they are not misinterpreted as real emission.

We re-edited some masks during kinematic modelling, for instance enlarging them by a pixel if they are too tight. Masks can be visualised in the position-velocity and channel map plots of $^{3D}BAROLO$, if the PLOTMASK parameter is set to TRUE. The mask boundary is plotted as a thick black line around the data. Models were improved further where possible, by adjusting and fixing the systemic velocity found by the source detection algorithm, after visually inspecting the P-V plots. Upon inspecting the moment maps of the output files, it was sometimes necessary to go back and readjust the coordinate centre points of the kinematic fits, from the estimates made by $^{3D}BAROLO$ by amounts smaller than the resolution of the images.

Initial estimates for the disc scale height parameter Z0 were taken to be zero at first, on the grounds that we assume our galaxies to be infinitely thin, with the low spatial resolution dominating over any intrinsic thickness (Di Teodoro et al. 2016). At a later point it was found that the models improved marginally by assuming a scale height of $\sim$ 300 parsec, which corresponds to approximately 0.035" $z \sim 2$.

4 Results & Discussions

In this section we present the kinematic models built by $^{3D}BAROLO$ for our galaxy sample. Multiple iterations were endured to improve the robustness and accuracy of the models, so that they follow the data as closely as possible. The blue contours in the position-velocity (P-V) plots (Figure 7) represent the data, and the red contours the model. The yellow dots on the diagrams represent the projected rotation velocities. The number and separation of the rings is given in Table 6. $^{3D}BAROLO$ offers two different methods of normalisation of the surface brightness, one being LOCAL in which the model is normalised pixel-by-pixel, and the second being AZIM, in which an azimuthal symmetry is forced upon the models. The models described in this section have been normalised locally. For reference the reader may see the azimuthal models in the appendix (Section 7).

In the channel maps, the thicker black line surrounding the emission shows the mask used in each case. Some masks are more constricting than others. For example, the mask for U3_5138 leaves more space around the emission, than the mask for GS4_37124. The galaxies with a lower signal-to-noise ratio required a tighter mask, to allow $^{3D}BAROLO$ to constrain the emission regions more reliably. Moment maps (see Figure 8) display the intensity of emission, the velocity field, and also the velocity dispersion in three rows of panels for the data, the model and the residual for each galaxy. The black dashed line in these diagrams represents the kinematic axis, and reflects the position angle of the galaxy. For all galaxies in the sample, both the approaching and receding sides are fitted together, which gave mostly good results for all galaxies in the sample. For the galaxy ZC407302, there is more of an asymmetry between each half (so-called lopsidedness), and so I fitted them separately to compare the fits. Section 7 shows the models made using the approaching and receding sides of the galaxy separately.

The models achieved are very realistic and allow for the recovery of meaningful kinematic information in most cases. Note that due to the low resolution of high-redshift imaging, where we find flat rotation curves these are only indicators, and not proof, that the galaxy has a rotation curve flat for all intermediate and larger radii. Below we address and discuss each model individually.

Sample Kinematics				
Galaxy ID	$Log(\frac{M_*}{M_\odot})$	$V_{flat}[km\ s^{-1}]$	Average σ $[km\ s^{-1}]$	$\frac{V_{flat}}{\sigma}$
COS3_18434	$10.59 \pm\ 0.18$	182^{+6}_{-5}	25^{+6}_{-6}	$7.4^{+1.7}_{-1.7}$
U3_5138	$9.72 \pm\ 0.47$	130^{+7}_{-8}	24^{+6}_{-6}	$5.5^{+1.4}_{-1.4}$
GS4_37124	$10.49 \pm\ 0.11$	178^{+11}_{-12}	69^{+7}_{-7}	$2.6^{+0.3}_{-0.3}$
ZC407302	$10.39 \pm\ 0.11$	174^{+25}_{-24}	61^{+11}_{-11}	$2.9^{+0.7}_{-0.7}$

Table 5: Information on the galaxy sample that I have used in my scaling relations. Stellar mass has been taken from literature, whereas V_{flat} and σ have been derived from the models.

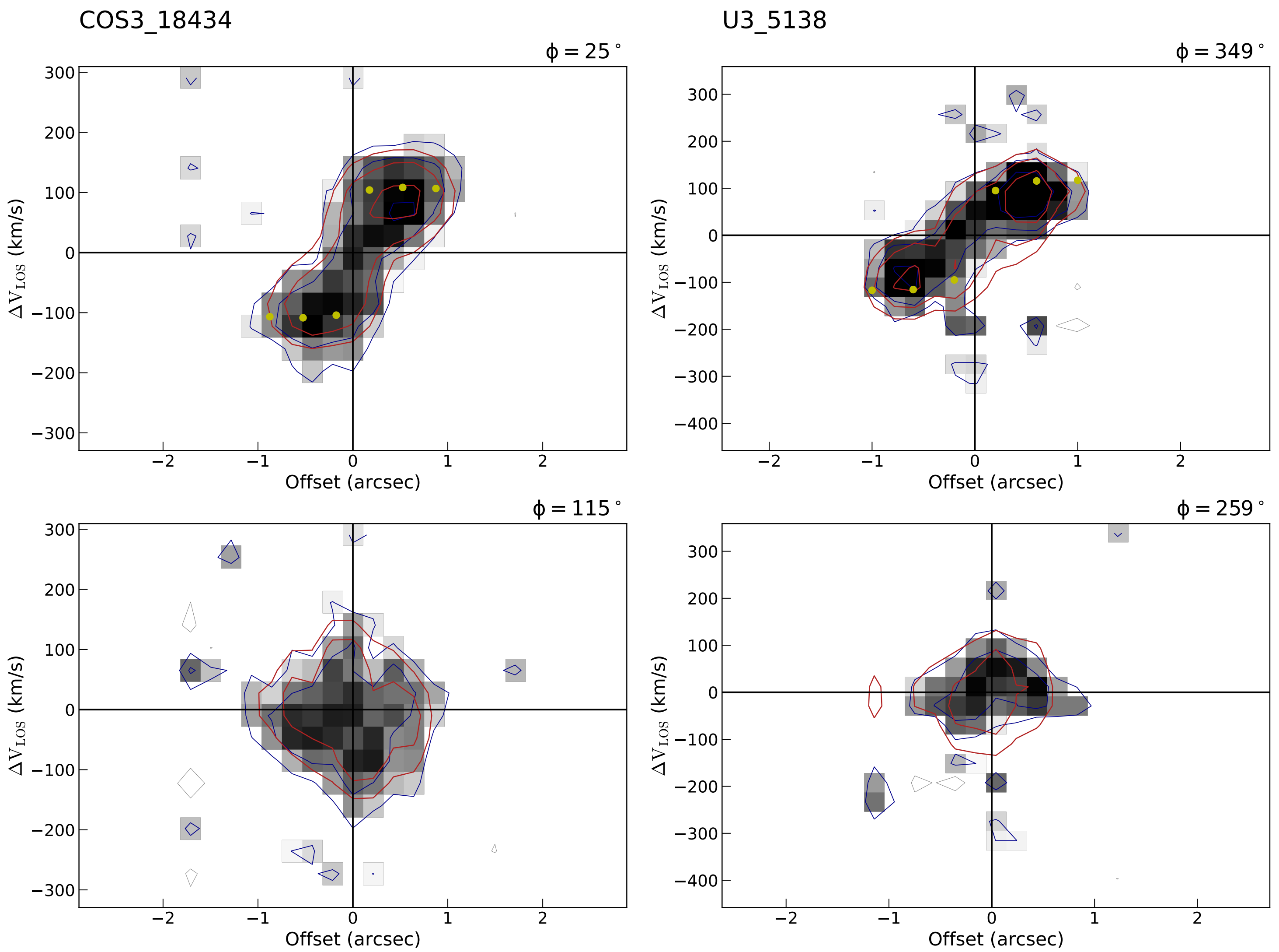

(a) COS3_18434

(b) U3_5138

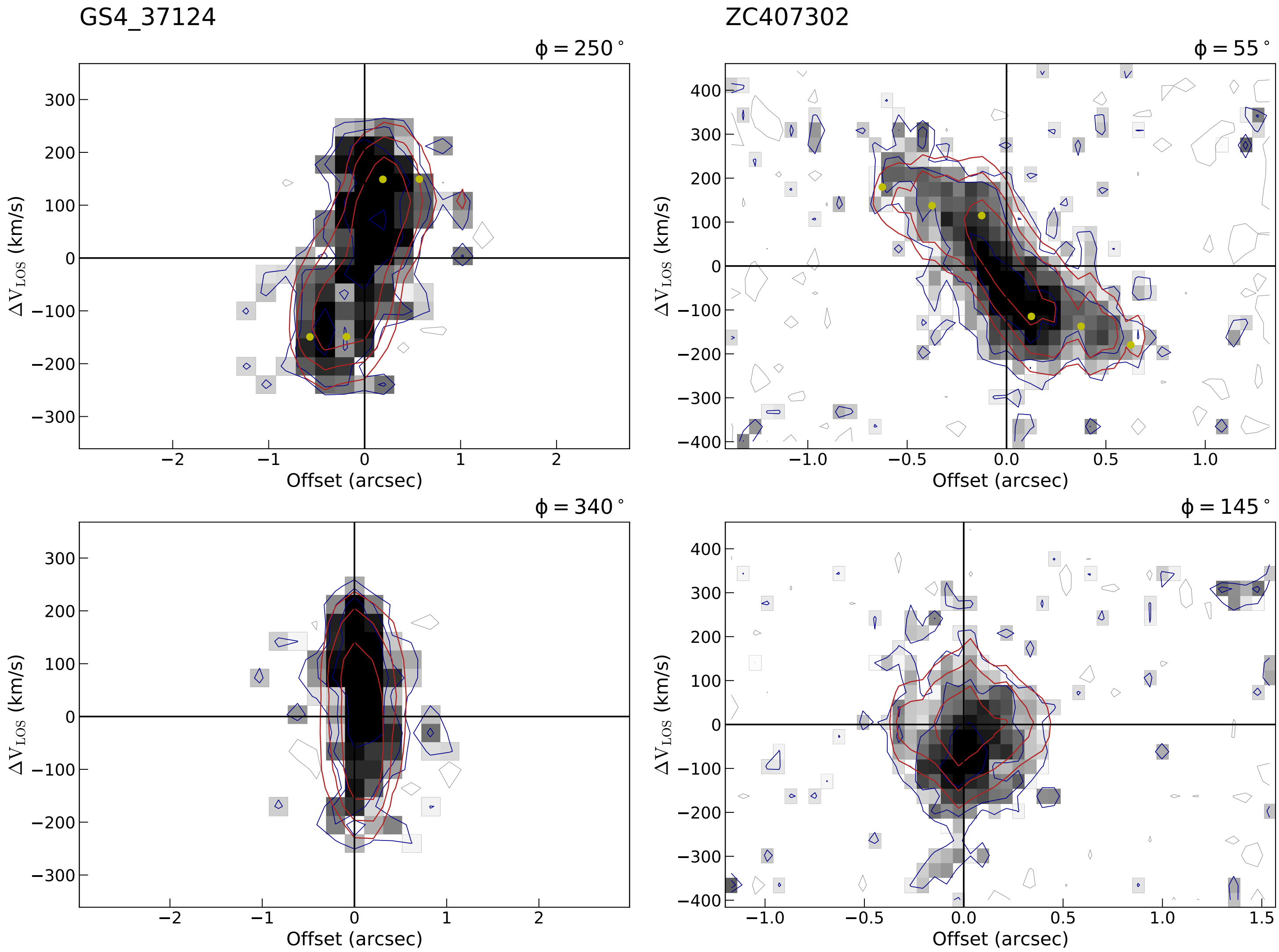

(c) GS4_37124

(d) ZC407302

Figure 7: Position - velocity plots from the $^{3D}BAROLO$ models, extracted along the major (upper panels) and minor (lower panels) axes. Grey-scale pixels show the emission, blue and grey contours show the data, and red contours the model, at levels of $2^n\sigma$ with grey showing the negative contours. Yellow points represent the projected rotation velocities.

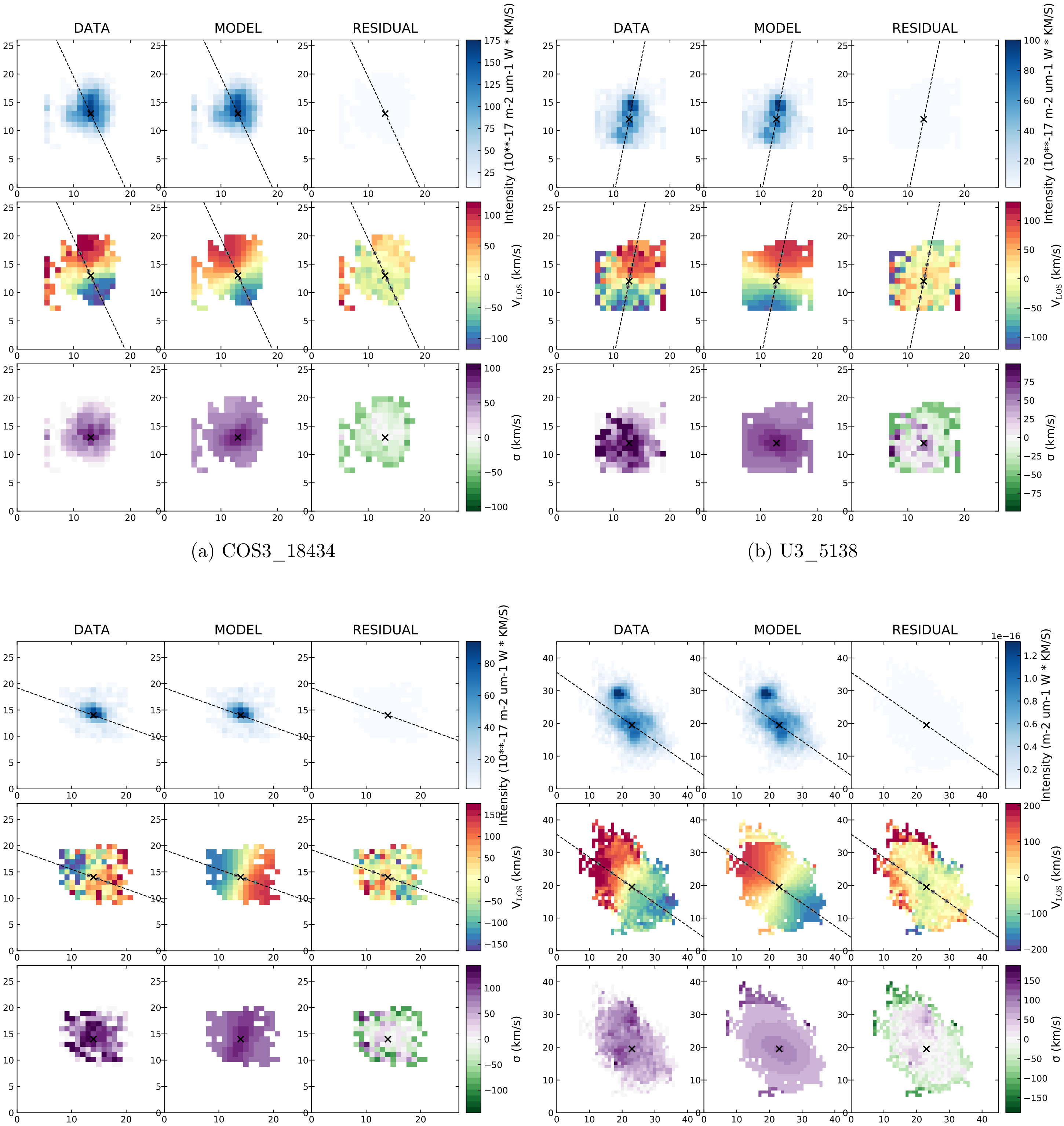

(a) COS3_18434 (b) U3_5138

(c) GS4_37124 (d) ZC407302

Figure 8: Moment map plots from the $^{3D}BAROLO$ models. The top panels show the 0th moment intensity map, the second row shows the 1st moment velocity map, and the third row shows the 2nd moment dispersion map.

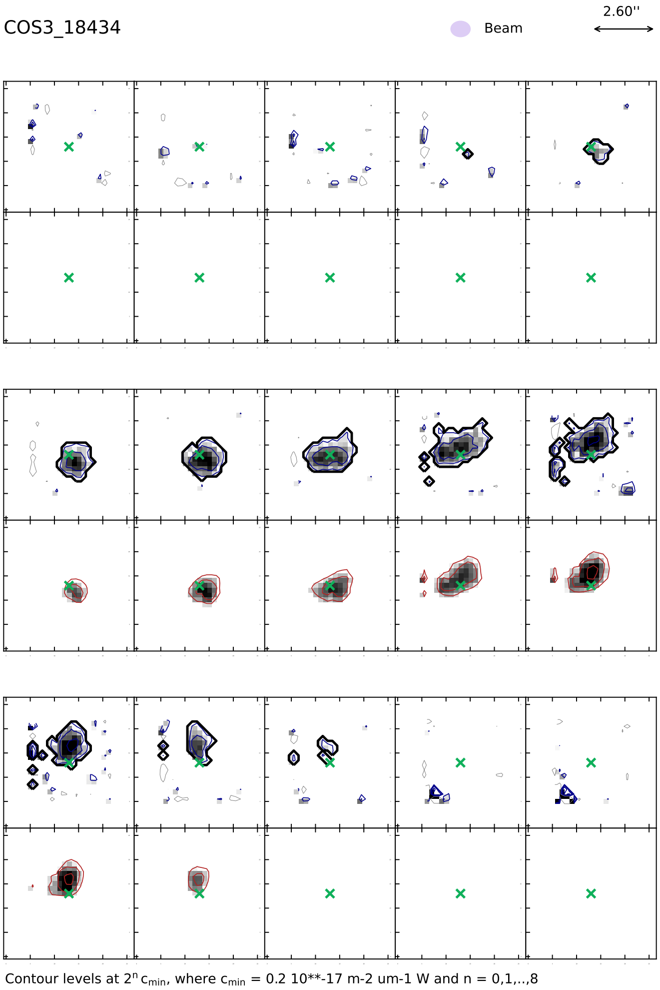

(a) COS3_18434

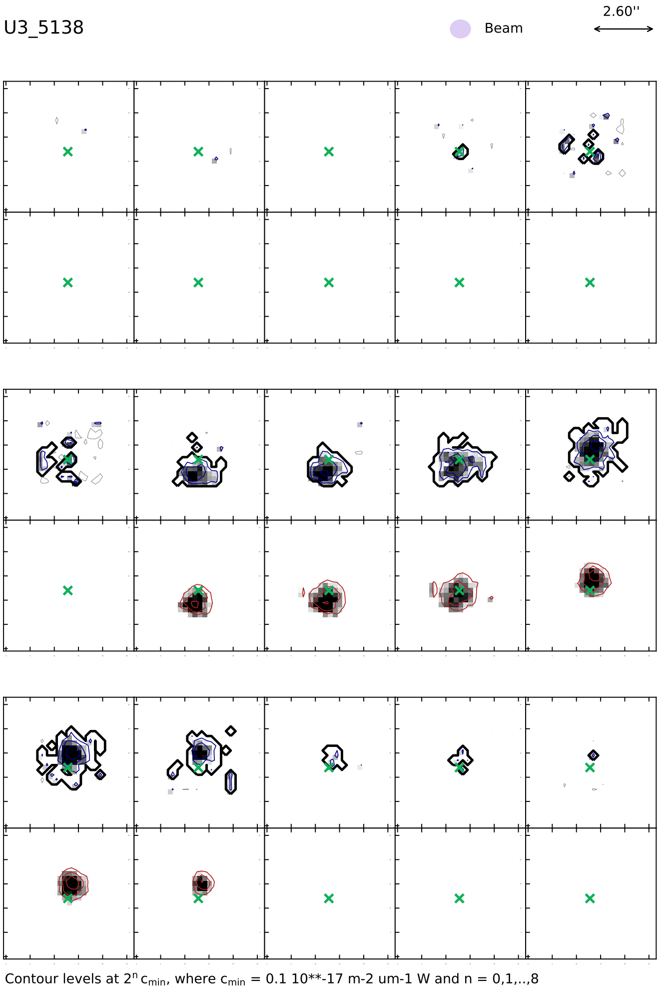

(b) U3_5138

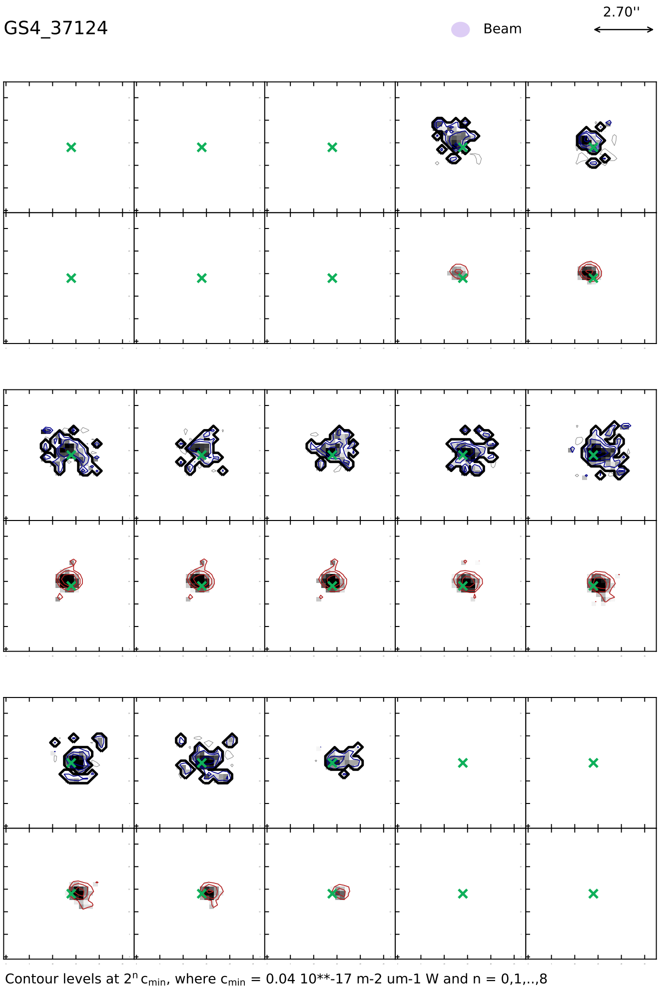

(c) GS4_37124

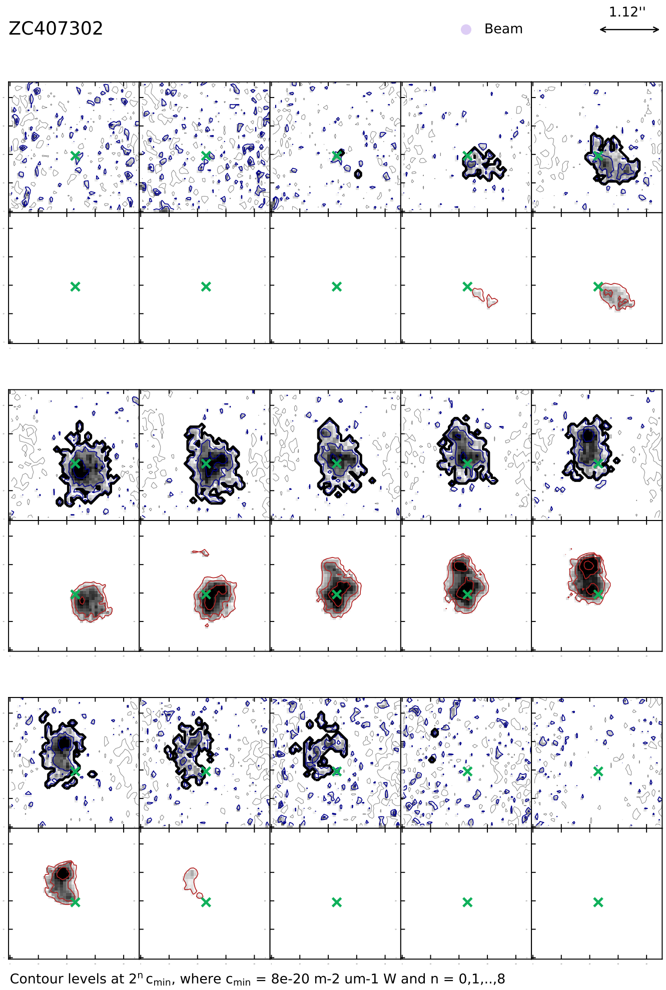

(d) ZC407302

Figure 9: Channel map plots from the $^{3D}BAROLO$ models, where upper panels with blue and grey contours show the data, and the lower panels with red contours show the corresponding model. Contours are plotted at levels of $2^n\sigma$, with grey contours being negative. The green cross shows the kinematic centre, and the thick black line shows the mask boundary.

Parameters			
Galaxy	N	RADSTEP ["]	Side fitted
COS3_18434	3	0.35	B
U3_5138	3	0.40	B
GS4_37124	2	0.38	B
ZC407302	3	0.26	B, A, R

Table 6: Key parameters used in the models. $^{3D}BAROLO$ fits N rings, each separated by RADSTEP. The side fitted is either the approaching (A), receding (R), or both together (B).

4.1 COS3_18434

Looking first at COS3_18434, it can be seen from the points in the P-V diagram (Figure 7a) that we find a rotation curve already flat by $\sim 0.1"$, or 0.8 kpc from the kinematic centre, suggesting it rises very steeply in the inner parts of the galaxy before reaching a plateau at $V_{flat} = 182^{+6}_{-5}$ km s^{-1}. Velocity dispersion oscillates marginally around the relatively low value of $\sigma = 25^{+6}_{-6}$ km s^{-1}, and very low residuals in the moment maps imply accurate models. In these moment maps one can observe a small region on the left-hand side, where noise has been included in the mask by the program. As it does not affect the body of the model it poses little issue. In the channel maps, one may observe that the model does not extend over perhaps one channel at either end of its emission spectrum, but this is no issue as the emission there is particularly faint, and hard to distinguish from the noise. Increasing the mask further in this case just allows unwanted noise into the data. The relatively low velocity dispersion leads to a fairly high V/σ ratio of over 7, implying this galaxy is highly rotation dominated.

4.2 U3_5138

Similarly for the second galaxy at $z \sim 1$, U3_5138, we find an indication of a flat rotation curve at $V_{flat} = 130^{+7}_{-8}$ km s^{-1}, and a consistently low average velocity dispersion of $\sigma = 24^{+6}_{-6}$ km s^{-1}. This was the galaxy that has already been modelled using $^{3D}BAROLO$ (Di Teodoro et al. 2016), where a rotation velocity $V_{flat} = 128 \pm 14$ km s^{-1} and an average velocity dispersion $<\sigma_{H\alpha}> = 24 \pm\ 6$ km s^{-1} were found, with a consequent V/σ ratio of ~ 4.9; reassuringly comparable to and within the errors of the values found in this study. The mask used for this fit is a little looser than in the previous galaxy, and consequently some regions that we would assume to be noise have been interpreted as emission. Again though, this is no issue as the model does not include these regions. In the channel maps (Figure 9b) there are a couple of channels in which the model has not perfectly reproduced the data at either side, yet the mask allows a small region in which there is no significant emission; not significant enough to meet the threshold for genuine emission.

4.3 GS4_37124

With GS4_37124, we only use two rings in the model. This was because there is not really room to use a third point, without severely oversampling the galaxy. A third point was tested, which lay very close to the centre and thus gave an unreliable rotation velocity close to zero. Regardless, this galaxy was found to have a possibly flat rotation curve at $V_{flat} = 178^{+11}_{-12}$ km s^{-1}, and a roughly constant velocity dispersion at approximately $\sigma = 69^{+7}_{-7}$ km s^{-1}. The dispersion is notably higher than in the galaxies at $z \sim 1$ and this causes the ratio V/σ to be the lowest of the four galaxies. However, as I only used two points it would be unreasonable to claim that the dispersion would be constant at other radii around the points, and so it may be overestimated. The channel maps in Figure 9c show how the model extends over all channels in which emission is present.

4.4 ZC407302

The galaxy ZC407302 presented more problems than the others during the modelling. First note the bright region above the main body of the galaxy in the moment maps (Figure 8d), possibly a merger or a bright star-forming region and not to be included in the model. Although not using $^{3D}BAROLO$, this galaxy has been modelled in previous literature (Förster Schreiber et al. 2018) and found to have a rotation velocity of $V_{rot} = 204^{+6}_{-6}$ km s^{-1}, and an average velocity dispersion $\sigma = 56^{+11}_{-25}$ km s^{-1}. We found a lower outer rotation velocity of $V_{flat} = 174^{+25}_{-24}$ km s^{-1}, but a similar average velocity dispersion $\sigma = 61^{+11}_{-11}$ km s^{-1} in the outer rings. The channel maps, and P-V diagram appear noisier than the other plots, but this is likely due to the fact that in $^{3D}BAROLO$ we used a lower threshold to better constrain the emission of the galaxy. The noise varies channel-by-channel, and is possibly a consequence of sky subtraction. It is also worth noting that this galaxy was taken from a different data set than the first three (see Section 2) and so the output plots may not look quite the same as the others.

The channel maps for this galaxy (Figure 9d) show that the receding side of the galaxy model does not produce the emission of the blue contours as the approaching side does, and so we model the approaching and receding sides independently (see Section 7). Figures 15 and 17 show the P-V diagrams and moment maps, and in these you can see that the model finds indications of a flat rotation curve for the approaching side, yet a continuously rising curve for the receding side with greater velocity dispersions overall. It is clear that the approaching side models the galaxy more accurately, finding an outer rotation velocity of $V_{flat} = 175^{+20}_{-22}$ km s^{-1}, and an average velocity dispersion among the rings of $\sigma = 65^{+8}_{-12}$ km s^{-1}. These values are very similar to, and within the errors of those found by the model that utilises both sides of the galaxy, and so the values in Table 5 are extracted from the first model (Figure 7d). The reasons for the more problematic model could be related to the intrinsic dynamical state or properties of the galaxy. One possibility is that the galaxy has a strong bar and the line-of-sight velocities in the central regions are not fully representative of the rotation, or bright star-forming regions with outflows that are offsetting the velocities from the rotation of the galaxy.

The azimuthal plots in Section 7 are not largely dissimilar to the locally-normalised ones we present in this section for the first three galaxies. The azimuthal model for ZC407302 however does appear less accurate, and we attribute this to the asymmetry between its approaching and receding sides. For the rest, the best-fitting parameters reach similar values, and the P-V plots are almost identical.

4.5 Rotation Curves

Figure 10a shows the rotation curves derived by $^{3D}BAROLO$ for the galaxies in this study. All rotation curves appear to reach a flat plateau at low radii, with the exception of ZC407302 for which the curve increases steadily from ~ 1 kpc to ~ 5 kpc, with higher uncertainties than the others. Figure 10b shows the velocity dispersions at the same radii, and the reader may note that most appear to be approximately constant, with no apparent trend with radius. The dispersion for ZC407302 on the other hand decreases with radius, but we may assume that dispersion in the outer ring may have a higher degree of uncertainty due to poorer resolution in the region. Using the kinematic information presented in this section, we can move on to study the galaxies in the context of scaling relations, and derive some more intrinsic properties.

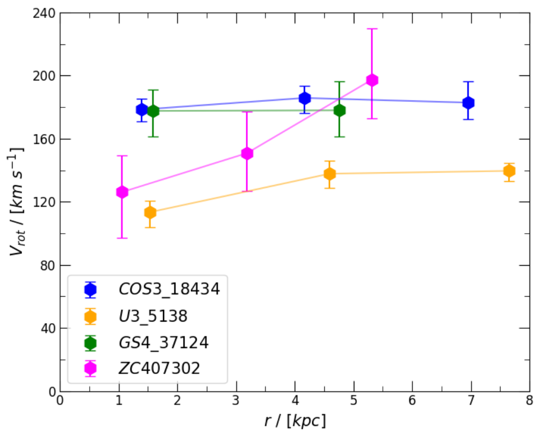

(a) Rotation velocities

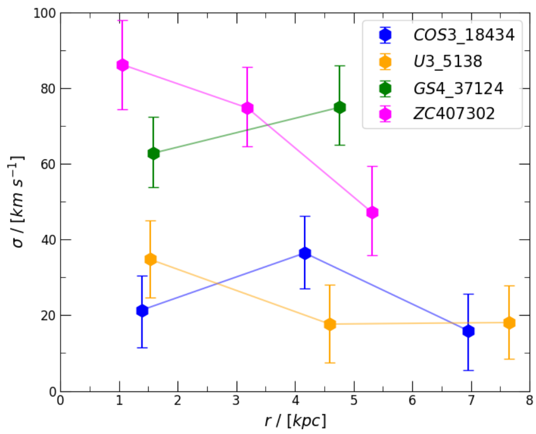

(b) Velocity dispersions

Figure 10: Rotation velocity and velocity dispersions derived by $^{3D}BAROLO$. The left panel shows the derived rotation curve, and the right panel shows the corresponding velocity dispersions, with their respective errors. The values of the parameters and their errors can be found in Table 6.

4.6 The Tully-Fisher Relation

Scaling relations for galaxies show trends between various physical properties of galaxies, and provide an insight into galaxy evolution and formation processes. One of the most prominent scaling relations for galaxies is the Tully-Fisher relation (Tully and Fisher 1977) between rotation velocity and intrinsic luminosity or stellar mass. Following Di Teodoro et al. 2016, the characteristic velocities of the flat part of the rotation curve, V_{flat}, are calculated by taking the average value of the rings modelled using $^{3D}BAROLO$ in the flat part of the curve. A Tully-Fisher best-fit relation follows the general form:

$$\log\left(\frac{M_*}{M_\odot}\right) = a + b\log\left(\frac{V_{flat}}{[km\ s^{-1}]}\right), \tag{3}$$

where the free parameters a & b represent the intercept and the slope of the best fit line. Figure 11 shows the stellar mass Tully-Fisher relation for the galaxies in this study. Figure 11a contains the two galaxies at $z \sim 1$, and Figure 11b those at $z \sim 2$. The grey points and their respective errors in Figure 11a are taken from Di Teodoro et al. 2016 and represent a galaxy sample at

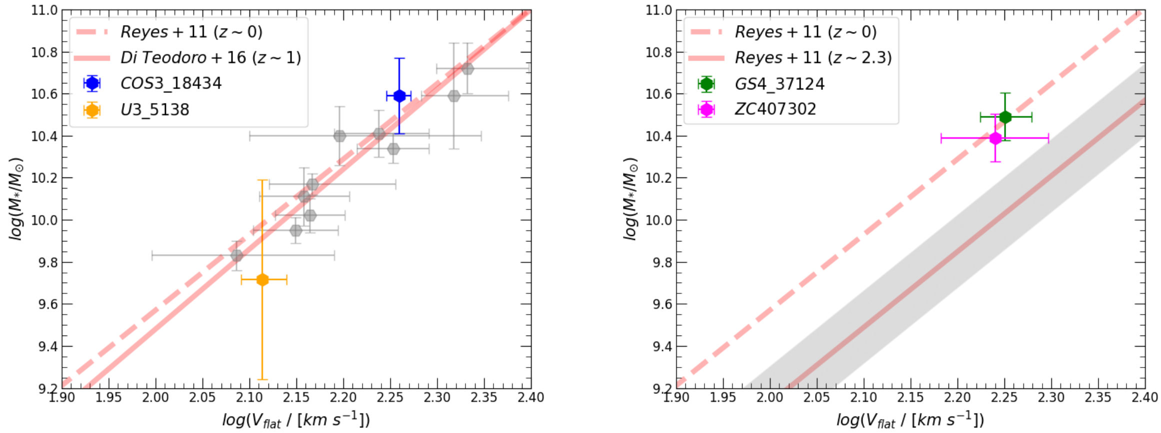

(a) $z \sim 1$ (b) $z \sim 2$

Figure 11: The stellar mass Tully-Fisher relation including our points at $z \sim 1$ in the left panel with points from Di Teodoro et al. 2016 in grey, along with their best fit line in solid red (parameters $a = 1.88, b = 3.80$). The right panels shows our sample at $z \sim 2$, with a best-fit line for a sample at $z \sim 2.3$ is taken from Reyes et al. 2011 and plotted as the solid red (parameters $a = 1.93, b = 3.60$) line, with its intrinsic scatter in grey. In both panels, the dashed red line represents the sample in Reyes et al. 2011 at $z \sim 0$ (parameters $a = 2.39, b = 3.59$).

$z \sim 1$, with the solid red line showing their best fit (parameters $a = 1.88, b = 3.80$). For comparison we show the best fit line from Reyes et al. 2011 for a study of galaxies at $z \sim 0$, shown as the dashed red line in both panels (parameters $a = 2.39, b = 3.59$). Also in Figure 11b, we plot the best-fit line for a galaxy sample at $z \sim 2.3$ (parameters $a = 1.93, b = 3.60$), also taken from Übler et al. 2017, where the grey bar represents an intrinsic scatter of 0.26 dex; the reader can clearly see that the two galaxies in our sample at $z \sim 2$ lie much closer to the $z \sim 0$ line that that at $z \sim 2.3$, suggesting no evolution of the TF relation with redshift.

As we only modelled four galaxies, we do not attempt to calculate a best-fit line for our sample, to try to infer any evolution of the zero point of the Tully-Fisher relation. The points from this study fall within reasonable bounds of the errors of the literature values, and on initial inspection it does seem to reflect no significant evolution of the Tully-Fisher relation from redshift $z \sim 0$ to $z \sim 2$. The larger error bar for the galaxy U3_5138 is due to the large discrepancy between values found in different literature for the galaxy's mass (See section 2).

4.7 Effective Radius and the Fall Relation

By definition, the scale length of an exponential surface profile of a galaxy is the radius at which the surface brightness has decreased by a factor e. From the scale length (See section 3.4), we can estimate the effective radius R_{eff} for an exponential disc using:

$$R_{eff} \approx R_d * (1.687) \tag{4}$$

As in Kirby et al. 2008, equation 7; this is the radius at which the luminosity of the galaxy is half of the maximum value, and the values found are shown in Table 7. Figure 12a shows a plot of V_{flat} vs R_{eff} for the galaxy sample. Sharma et al. 2020 found in their study that in the

$z \sim 0$ regime, there was a distinct proportionality between V_{flat} vs R_{eff}, yet at $z \sim 1$, R_{eff} was approximately constant for all values of V_{flat} up to ~ 220 km s^{-1}. In our study, we find no such relation, and no apparent correlation between redshift, effective radius and rotation velocity.

Parameters derived from Surface Brightness Profiles and Kinematic Models			
Galaxy ID	R_e [kpc]	R_d [kpc]	j_* [kpc km s^{-1}]
COS3_18434	2.90 ± 0.06	1.71 ± 0.03	371^{+14}_{-13}
U3_5138	5.01 ± 0.07	2.97 ± 0.04	460^{+26}_{-29}
GS4_37124	3.70 ± 0.07	2.19 ± 0.04	465^{+30}_{-33}
ZC407302	5.61 ± 0.34	3.33 ± 0.20	690^{+108}_{-104}

Table 7: Information on the galaxy sample derived from the fitted exponential intensity profiles.

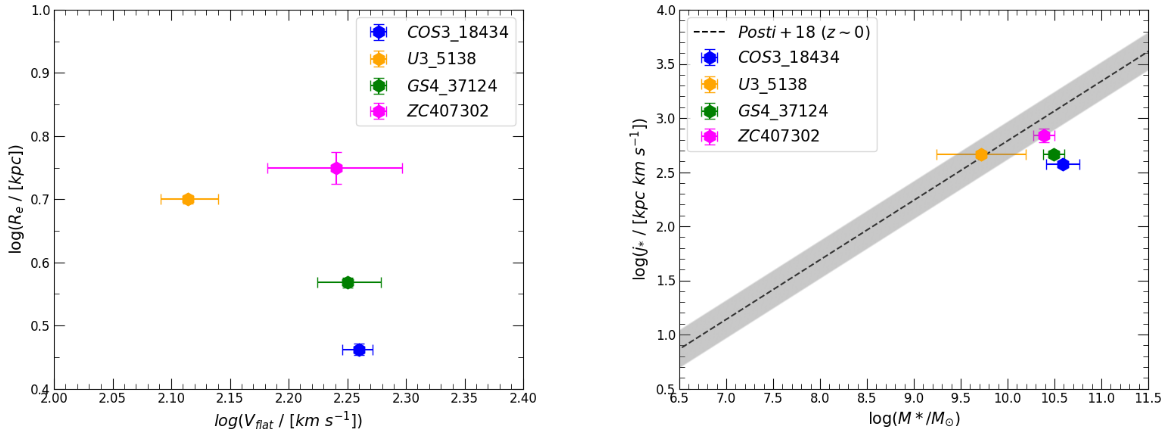

(a) Effective radius R_{eff} derived from the scale length R_d, versus rotation velocity, plotted following the relation in Sharma et al. 2020.

(b) The Fall relation between stellar-specific angular momentum and stellar mass (Fall 1983), with best-fit line from Posti et al. 2018 for spiral galaxies at $z \sim 0$, with the grey bar representing the 1σ orthogonal intrinsic scatter of 0.17 dex.

Figure 12: Relations for the galaxy sample in this study, including a plot of effective radius versus rotation velocity as in Sharma et al. 2020, and the Fall relation.

The relation between the specific stellar angular momentum and stellar mass (Fall 1983; Posti et al. 2018; Marasco et al. 2019), sometimes called the Fall relation, is a very important scaling relation involving fundamental parameters of galaxies, and is a benchmark of galaxy evolution models. For an exponential disc with flat rotation curve, the stellar specific angular momentum, j_*, is given, to a very good approximation (Posti et al. 2018), by:

$$j_* = 2 * R_d * V_{flat}. \tag{5}$$

Figure 12b shows the galaxy sample from this study plotted in a Fall relation, with a line of best fit from Posti et al. 2018 for spiral galaxies at $z \sim 0$, with the grey bar representing the 1σ

orthogonal intrinsic scatter of 0.17 dex. The figure shows two of the four galaxies in this sample lie well within the bounds of the best-fit line, including their errors. The other two lie below the 0.17dex intrinsic scatter, one at $z \sim 1$ and the other at $z \sim 2$, so we cannot draw any conclusions concerning redshift evolution.

5 Conclusions

This study saw the application of the relatively new code $^{3D}BAROLO$ to four low-resolution Hα emission-line data cubes, taken from the KMOS3D and SINS galaxy surveys, at redshifts ranging between $z \sim 0.8$ and $z \sim 2.4$. Advantageous to our method, the three-dimensional tilted ring approach overcomes the influence beam smearing exerts on traditional two-dimensional models, which generally causes the under- and over- estimation of rotation velocity and velocity dispersion respectively. We have demonstrated the capabilities of $^{3D}BAROLO$ to model particularly poorly resolved cubes, in scenarios where two-dimensional models would likely fail to accurately derive intrinsic kinematics.

Prior to the kinematic modelling of the sample, we derived the parameters of the PSF of each of the data cube, by fitting two-dimensional Gaussian functions to the PSF images and extracting position angles and FWHM values along each axis. We fitted elliptical isophote models to the HST image of each of the galaxies, and thus determined their position angles and inclinations. Information from the same profiles was used to construct surface brightness profiles for the sample, from which further parameters including scale length and effective radius were derived.

We derived rotation curves and intrinsic velocity dispersions for our sample, and showed that the morphological properties of the galaxies are similar to those of galaxies in the local Universe. Rotation curves appear to rise sharply in the inner regions before flattening off around a maximum rotation velocity. However, we remind the reader that due to the low-resolution of the data, the derived curves are quite uncertain. Regardless, all of the galaxies appeared to display the properties of rotation-dominated discs with V/σ ratios greater than 2.5, with velocity dispersions higher for galaxies of higher redshift.

We report no significant evolution of the stellar mass Tully-Fisher relation, in gradient or zero-point, at all redshifts, yet with only four galaxies in the sample it would be unfair to draw any strong conclusions on scaling relation evolution. All four lay within acceptable error bounds of the line found for $z \sim 0$ by Reyes et al. 2011. Similarly, we placed our sample in a Fall relation and found that two of our galaxies lie within the error of the best-fit line found for $z \sim 0$ in Posti et al. 2018, and the other two lie just outside; more evidence for little evolution with redshift.

6 References

Bibliography

[SRR73] GS Shostak, DH Rogstad, and AH Rots. "APERTURE SYNTHESIS STUDY OF NEUTRAL HYDROGEN IN GALAXIES NGC-6946 AND IC-342". English. In: *Astronomy & astrophysics* 22.1 (1973), pp. 111–119. ISSN: 0004-6361.

[TF77] R.~B. Tully and J.~R. Fisher. "Reprint of 1977A&A....54..661T. A new method of determining distance to galaxies." In: *AaP* 500 (Feb. 1977), pp. 105–117.

[Bos78] A. Bosma. "The distribution and kinematics of neutral hydrogen in spiral galaxies of various morphological types". PhD thesis. -, Jan. 1978.

[RFT80] V.~C. Rubin, Jr. Ford W.~K., and N. Thonnard. "Rotational properties of 21 SC galaxies with a large range of luminosities and radii, from NGC 4605 (R=4kpc) to UGC 2885 (R=122kpc)." In: *apj* 238 (June 1980), pp. 471–487. DOI: 10.1086/158003.

[Fal83] S.~ M Fall. "Galaxy formation - Some comparisons between theory and observation". In: *Internal Kinematics and Dynamics of Galaxies*. Ed. by E. Athanassoula. Vol. 100. IAU Symposium. Jan. 1983, pp. 391–398.

[van+85] T. S. van Albada et al. "Distribution of dark matter in the spiral galaxy NGC 3198." In: *ApJ* 295 (Aug. 1985), pp. 305–313. DOI: 10.1086/163375.

[Beg89] K.~ G. Begeman. "HI rotation curves of spiral galaxies. I. NGC 3198." In: *AaP* 223 (Oct. 1989), pp. 47–60.

[Goo95] R. Gooch. "Space and the Spaceball". In: *Astronomical Data Analysis Software and Systems IV*. Ed. by R. A. Shaw, H. E. Payne, and J. J. E. Hayes. Vol. 77. Astronomical Society of the Pacific Conference Series. Jan. 1995, p. 144.

[Hay99] S. Churchman Haynes. *Rotation Curves*. 1999. URL: http://hosting.astro.cornell.edu/academics/courses/astro201/rotation_curves.htm.

[Ver01] Marc A.~W. Verheijen. "The Ursa Major Cluster of Galaxies. V. H I Rotation Curve Shapes and the Tully-Fisher Relations". In: *apj* 563.2 (Dec. 2001), pp. 694–715. DOI: 10.1086/323887. arXiv: astro-ph/0108225 [astro-ph].

[Boe+04] A. Boehm et al. "The tully-fisher relation at intermediate redshift". In: *Astron. Astrophys.* 420 (2004), pp. 97–114. DOI: 10.1051/0004-6361:20034256. arXiv: astro-ph/0309263.

[F+06] N.~M. Förster Schreiber et al. "SINFONI Integral Field Spectroscopy of z ~2 UV-selected Galaxies: Rotation Curves and Dynamical Evolution". In: *apj* 645.2 (July 2006), pp. 1062–1075. DOI: 10.1086/504403. arXiv: astro-ph/0603559 [astro-ph].

[PSL07] Laura Portinari and Jesper Sommer-Larsen. "The Tully–Fisher relation and its evolution with redshift in cosmological simulations of disc galaxy formation". In: *Monthly Notices of the Royal Astronomical Society* 375.3 (Jan. 2007), pp. 913–924. ISSN: 0035-8711. DOI: 10.1111/j.1365-2966.2006.11348.x. eprint: https://academic.oup.com/mnras/article-pdf/375/3/913/3934671/mnras0375-0913.pdf. URL: https://doi.org/10.1111/j.1365-2966.2006.11348.x.

[Kir+08] Emma M. Kirby et al. "DEEP NEAR-INFRARED SURFACE PHOTOMETRY OF 57 GALAXIES IN THE LOCAL SPHERE OF INFLUENCE". In: *The Astronomical Journal* 136.5 (Oct. 2008), pp. 1866–1888. DOI: `10.1088/0004-6256/136/5/1866`. URL: `https://doi.org/10.1088%2F0004-6256%2F136%2F5%2F1866`.

[Rey+11] R. Reyes et al. "Calibrated Tully-Fisher relations for improved estimates of disc rotation velocities". In: *mnras* 417.3 (Nov. 2011), pp. 2347–2386. DOI: `10.1111/j.1365-2966.2011.19415.x`. arXiv: `1106.1650 [astro-ph.CO]`.

[Wuy+11] Stijn Wuyts et al. "ON STAR FORMATION RATES AND STAR FORMATION HISTORIES OF GALAXIES OUT TOz∼ 3". In: *The Astrophysical Journal* 738.1 (Aug. 2011), p. 106. DOI: `10.1088/0004-637x/738/1/106`. URL: `https://doi.org/10.1088%2F0004-637x%2F738%2F1%2F106`.

[MD14] Piero Madau and Mark Dickinson. "Cosmic Star-Formation History". In: *Annual Review of Astronomy and Astrophysics* 52.1 (Aug. 2014), 415–486. ISSN: 1545-4282. DOI: `10.1146/annurev-astro-081811-125615`. URL: `http://dx.doi.org/10.1146/annurev-astro-081811-125615`.

[DF15] E. M. Di Teodoro and F. Fraternali. "^{3D} BAROLO: a new 3D algorithm to derive rotation curves of galaxies". In: *mnras* 451.3 (Aug. 2015), pp. 3021–3033. DOI: `10.1093/mnras/stv1213`. arXiv: `1505.07834 [astro-ph.GA]`.

[Wis+15] E. Wisnioski et al. "The KMOS^{3D} Survey: Design, First Results, and the Evolution of Galaxy Kinematics from 0.7 <= z <= 2.7". In: *The Astrophysical Journal* 799.2, 209 (Feb. 2015), p. 209. DOI: `10.1088/0004-637X/799/2/209`. arXiv: `1409.6791 [astro-ph.GA]`.

[Ade+16] P. A. R. Ade et al. "Planck2015 results". In: *Astronomy & Astrophysics* 594 (Sept. 2016), A13. ISSN: 1432-0746. DOI: `10.1051/0004-6361/201525830`. URL: `http://dx.doi.org/10.1051/0004-6361/201525830`.

[DTFM16] E. M. Di Teodoro, F. Fraternali, and S. H. Miller. "Flat rotation curves and low velocity dispersions in KMOS star-forming galaxies at z 1". In: *Astronomy & Astrophysics* 594 (Oct. 2016), A77. ISSN: 1432-0746. DOI: `10.1051/0004-6361/201628315`. URL: `http://dx.doi.org/10.1051/0004-6361/201628315`.

[Rod+16] M. Rodrigues et al. "Morpho-kinematics of z 1 galaxies probe the hierarchical scenario". In: *Monthly Notices of the Royal Astronomical Society* 465.1 (Oct. 2016), pp. 1157–1180. ISSN: 0035-8711. DOI: `10.1093/mnras/stw2711`. eprint: `https://academic.oup.com/mnras/article-pdf/465/1/1157/8593309/stw2711.pdf`. URL: `https://doi.org/10.1093/mnras/stw2711`.

[Til+16] Alfred L. Tiley et al. "The KMOS Redshift One Spectroscopic Survey (KROSS): the Tully–Fisher relation at z 1". In: *Monthly Notices of the Royal Astronomical Society* 460.1 (Apr. 2016), pp. 103–129. ISSN: 0035-8711. DOI: `10.1093/mnras/stw936`. eprint: `https://academic.oup.com/mnras/article-pdf/460/1/103/8115081/stw936.pdf`. URL: `https://doi.org/10.1093/mnras/stw936`.

[Gen+17] R. Genzel et al. "Strongly baryon-dominated disk galaxies at the peak of galaxy formation ten billion years ago". In: *Nature* 543.7645 (Mar. 2017), 397–401. ISSN: 1476-4687. DOI: `10.1038/nature21685`. URL: `http://dx.doi.org/10.1038/nature21685`.

[Ior+17] G. Iorio et al. "LITTLE THINGS in 3D: robust determination of the circular velocity of dwarf irregular galaxies". In: *mnras* 466.4 (Apr. 2017), pp. 4159–4192. DOI: 10.1093/mnras/stw3285. arXiv: 1611.03865 [astro-ph.GA].

[Pon+17] Anastasia Ponomareva et al. "From light to baryonic mass: The effect of the stellar mass-to-light ratio on the Baryonic Tully-Fisher relation". In: *Monthly Notices of the Royal Astronomical Society* 474 (Nov. 2017). DOI: 10.1093/mnras/stx3066.

[Üb+17] H. Übler et al. "The Evolution of the Tully–Fisher Relation between $z \sim 2.3$ and $z \sim 0.9$ with KMOS3D". In: *The Astrophysical Journal* 842.2 (June 2017), p. 121. ISSN: 1538-4357. DOI: 10.3847/1538-4357/aa7558. URL: http://dx.doi.org/10.3847/1538-4357/aa7558.

[Fö+18] N. M. Förster Schreiber et al. "The SINS/zC-SINF Survey of z ∼ 2 Galaxy Kinematics: SINFONI Adaptive Optics–assisted Data and Kiloparsec-scale Emission-line Properties". In: *The Astrophysical Journal Supplement Series* 238.2 (Oct. 2018), p. 21. DOI: 10.3847/1538-4365/aadd49. URL: https://doi.org/10.3847%2F1538-4365%2Faadd49.

[Pos+18] Lorenzo Posti et al. "The angular momentum-mass relation: a fundamental law from dwarf irregulars to massive spirals". In: *aap* 612, L6 (May 2018), p. L6. DOI: 10.1051/0004-6361/201833091. arXiv: 1804.04663 [astro-ph.GA].

[Pri+18] A. M. Price-Whelan et al. "The Astropy Project: Building an Open-science Project and Status of the v2.0 Core Package". In: *aj* 156, 123 (Sept. 2018), p. 123. DOI: 10.3847/1538-3881/aabc4f.

[Mar+19] A. Marasco et al. "The angular momentum of disc galaxies at z = 1". English. In: *Astronomy & astrophysics* 621 (Jan. 2019). ISSN: 0004-6361. DOI: 10.1051/0004-6361/201834456.

[Üb+19] Übler, H. et al. "The Evolution and Origin of Ionized Gas Velocity Dispersion from z 2.6 to z 0.6 with KMOS3D". In: *The Astrophysical Journal* 880.1 (July 2019), p. 48. ISSN: 1538-4357. DOI: 10.3847/1538-4357/ab27cc. URL: http://dx.doi.org/10.3847/1538-4357/ab27cc.

[MP+20] Pavel E Mancera Piña et al. "Robust Hi kinematics of gas-rich ultra-diffuse galaxies: hints of a weak-feedback formation scenario". In: *Monthly Notices of the Royal Astronomical Society* 495.4 (May 2020), pp. 3636–3655. ISSN: 0035-8711. DOI: 10.1093/mnras/staa1256. eprint: https://academic.oup.com/mnras/article-pdf/495/4/3636/33347788/staa1256.pdf. URL: https://doi.org/10.1093/mnras/staa1256.

[Sha+20] Gauri Sharma et al. *Flat Rotation Curves of $z \sim 1$ Star-Forming Galaxies and Evidence of Disk-Scale Length Evolution*. 2020. arXiv: 2005.00279 [astro-ph.GA].

7 Appendix

In this section we give additional figures, in support of the previous sections. First, we show the P-V diagrams for all four galaxies modelled in ${}^{3D}BAROLO$ using the azimuthal surface brightness normalisation, followed by the models made for the approaching and receding sides of the galaxy ZC407302 (see Section 4.4).

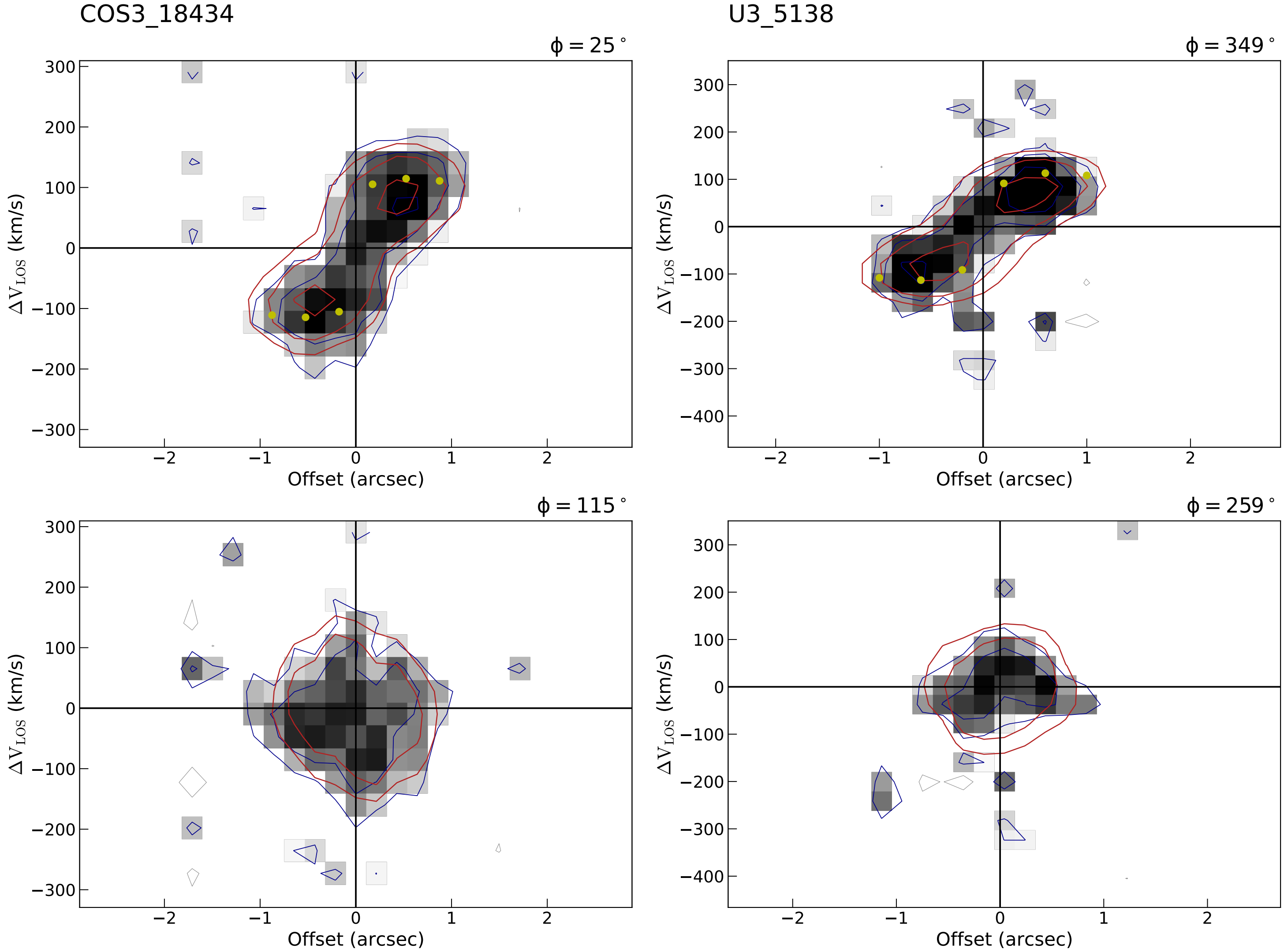

(a) COS3_18434 (b) U3_5138

Figure 13: Position - velocity plots from the azimuthally normalised ${}^{3D}BAROLO$ models, extracted along the major (upper panels) and minor (lower panels) axes for the two galaxies in this sample at $z \sim 1$. Grey-scale pixels show the emission, blue and grey contours show the data, and red contours the model, at levels of $2^n\sigma$ with grey showing the negative contours. Yellow points represent the projected rotation velocities.

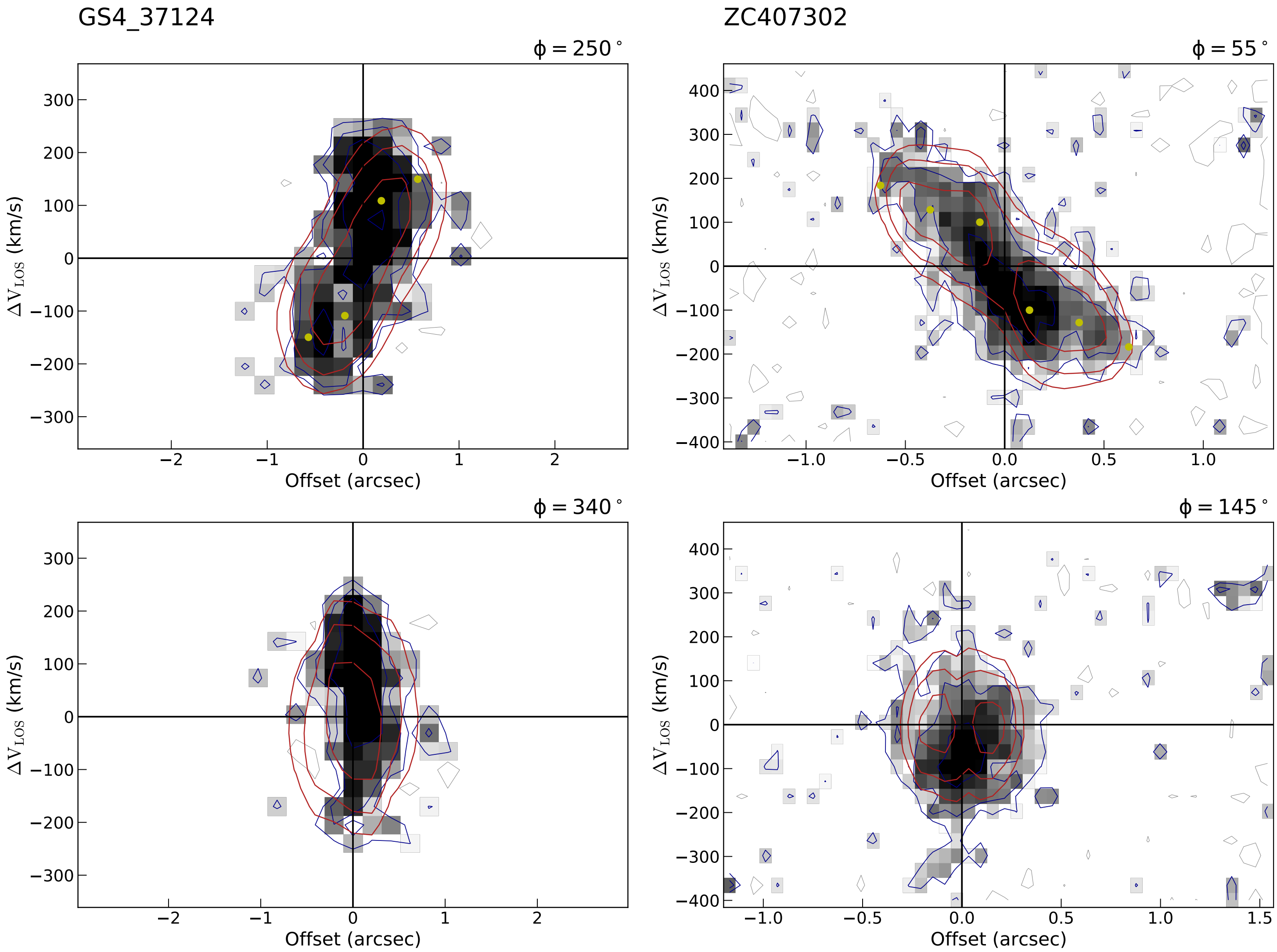

(a) GS4_37124 (b) ZC407302

Figure 14: A continuation of the previous figure, for the two galaxies in this sample at $z \sim 2$.

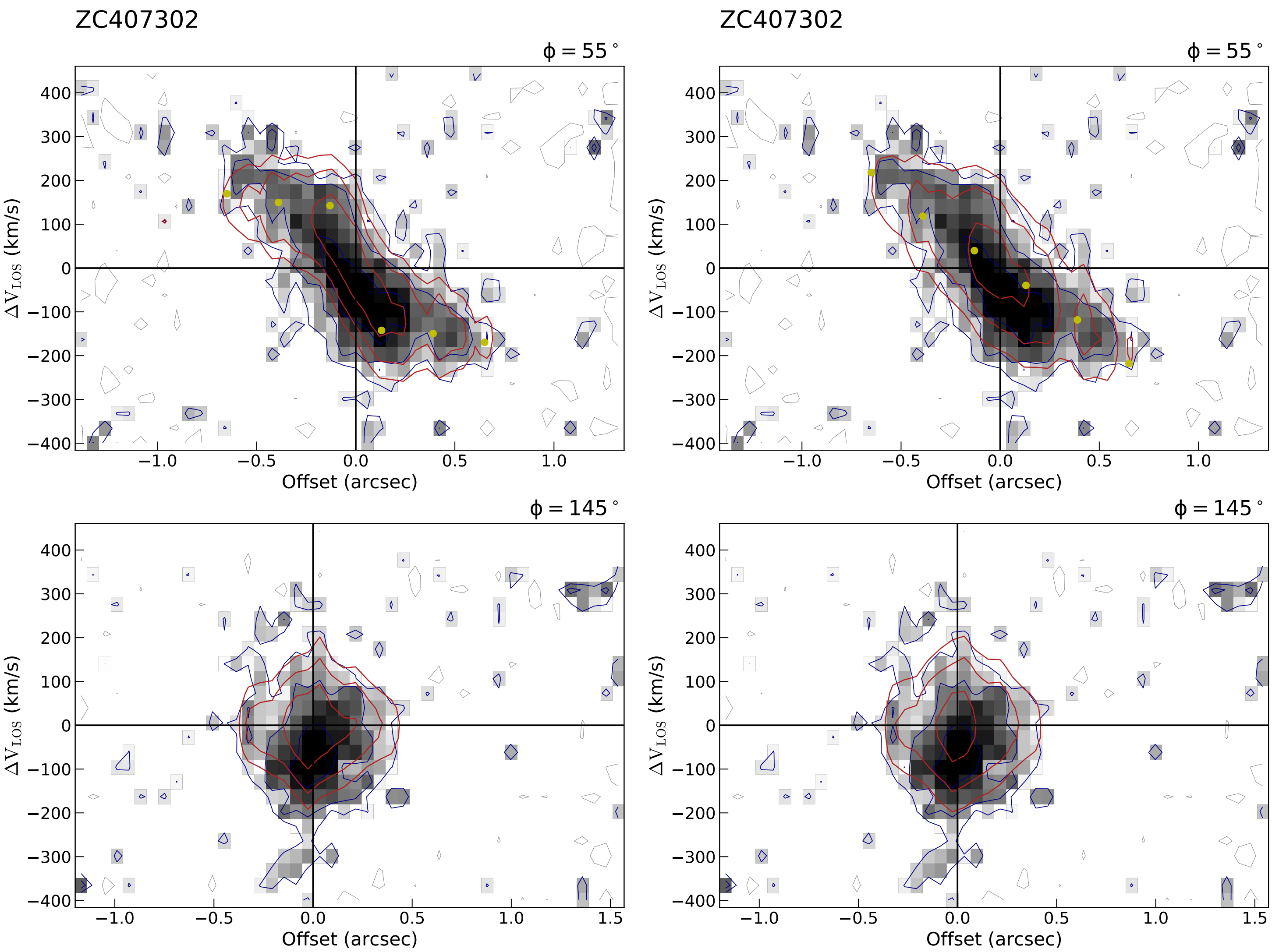

(a) Approaching (b) Receding

Figure 15: Position - velocity plots from the approaching and receding sides of the galaxy ZC407302, extracted along the major (upper panels) and minor (lower panels) axes. Grey-scale pixels show the emission, blue contours show the data, and red contours the model, at levels of $2^n\sigma$ with grey showing the negative contours. Yellow points represent the projected rotation velocities.

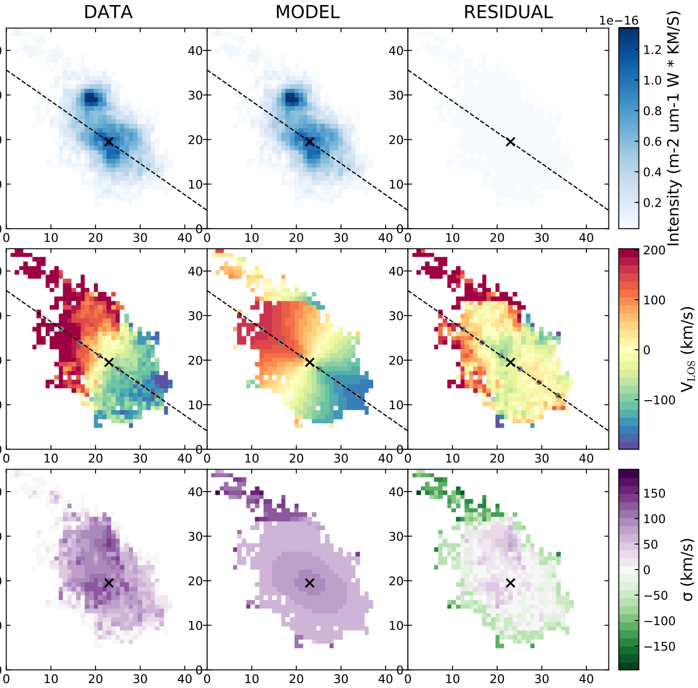

(a) Approaching

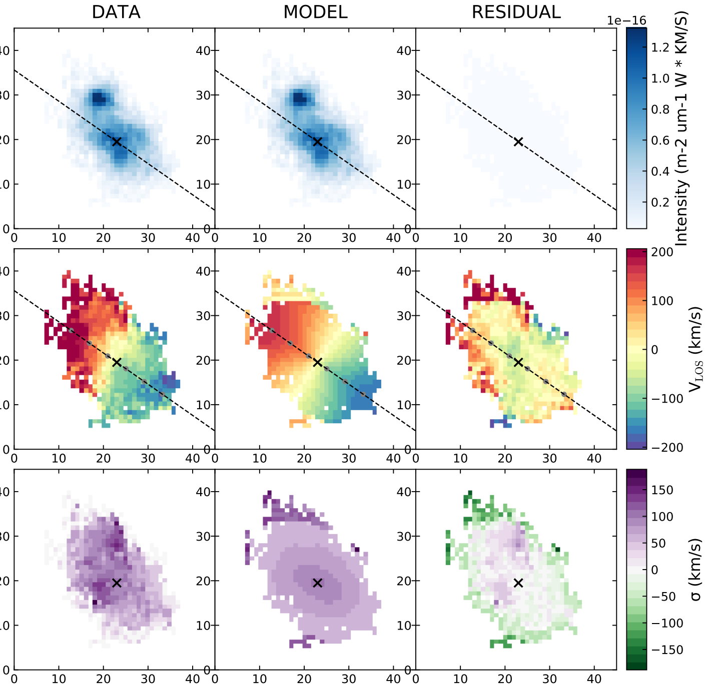

(b) Receding

Figure 16: Channel maps for the approaching and receding sides of ZC407302, where upper panels with blue and grey contours show the data, and the lower panels with red contours show the corresponding model, at levels of $2^n\sigma$ with grey showing the negative contours. The green cross shows the kinematic centre, and the thick black line shows the mask boundary.

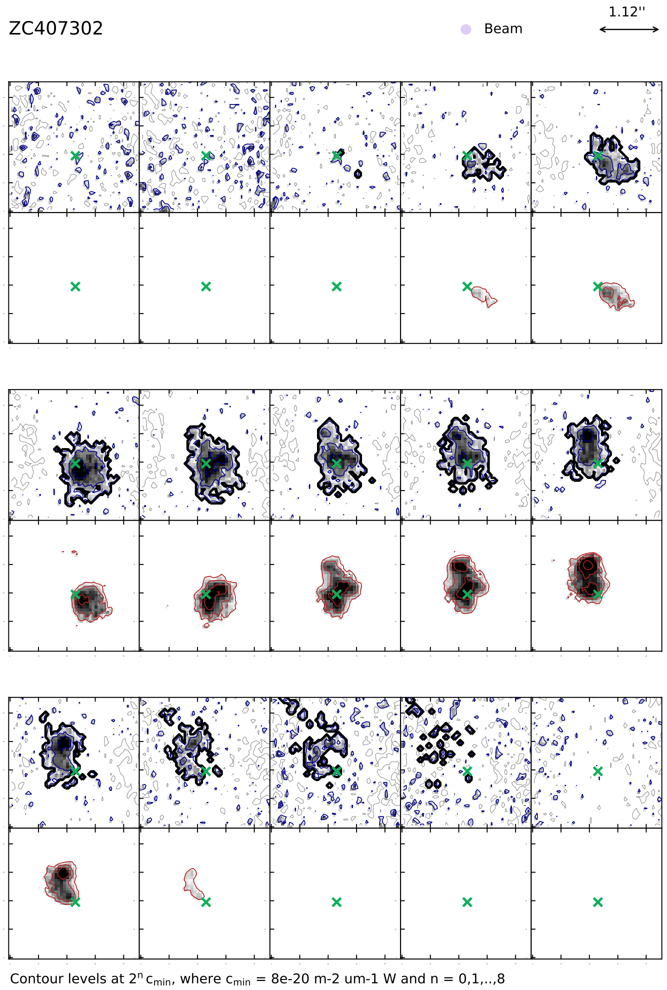

(a) Approaching

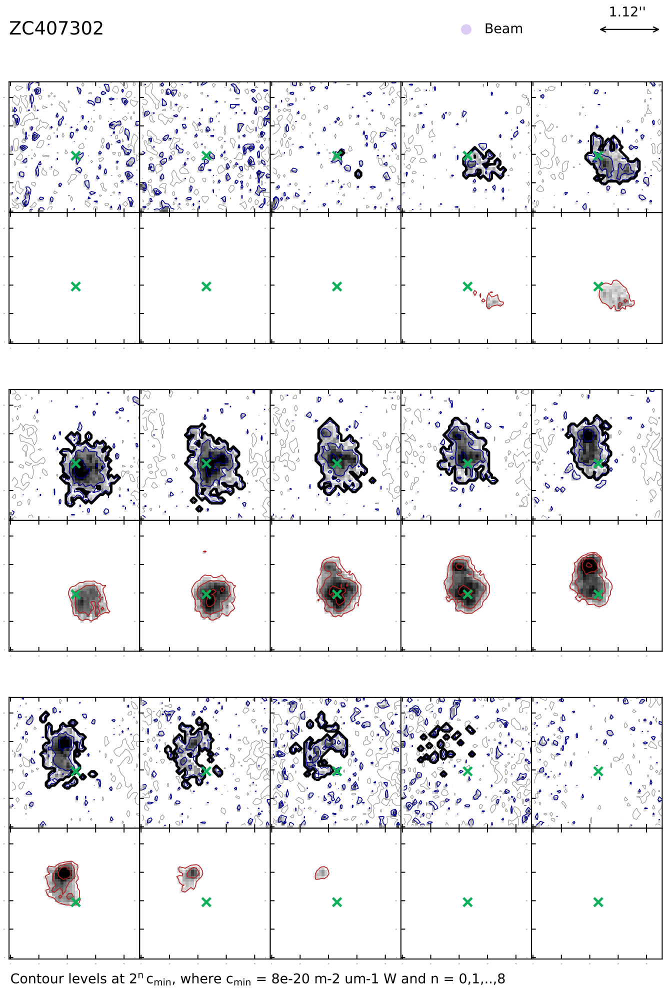

(b) Receding

Figure 17: Moment maps for the approaching and receding sides of ZC407302. The top panels show the 0th moment intensity map, the second row shows the 1st moment velocity map, and the third row shows the 2nd moment dispersion map.